國立臺灣大學理學院物理學系

碩士論文

Department of Physics

College of Science

National Taiwan University

master thesis

次毫米波干涉陣列影像相位修正策略

Phase Compensation Scheme for ACA Using SMA

陳育霖

Chen, Yu-Lin

指導教授：黃克寧博士

Advisor：Huang, Keh-Ning, Ph.D.

共同指導教授：松下聡樹博士

Coadvisor：Matsushita, Satoki, Ph.D.

中華民國 97 年 7 月

July, 2008

謝誌

這篇論文完成，得感謝很多人。首先是中研院天文所的松下聡樹博士不辭辛勞的教誨以及超人的耐心，次毫米波干涉陣列(SMA)研究群的成員提供聰明的想法。黃克寧老師給我許多理論物理學家的見解，讓我見識理論物理的無遠弗屆，黃俊峰學長給予建議和加油。接著則是要感謝高桑繁久博士，給我許多珍貴的建議。

最後還要感謝原分所原子物理 219 實驗室的成員們給我的幫助和打氣。以及支持我的家人。

中文摘要

毫米(millimeter)與次毫米波(Submillimeter)提供了宇宙中低溫塵埃輻射與許多分子光譜資訊，是地面天文觀測最後的波段。建造當中的新一代地表最大次毫米波干涉儀（the Atacama Large Millimeter and submillimeter Array，簡稱 ALMA）是有史以來最大的地面望遠鏡興建計畫。毫米和次毫米波的干涉影像相位起伏擾動主要都是受到對流層水汽分布的影響。為了減低觀測影像相位擾動，我們使用夏威夷白山(Mauna Kea)上的次毫米波干涉陣列（Submillimeter Array，簡稱 SMA）的觀測數據來發展相位補償修正策略，以作為最大次毫米波干涉儀 ALMA 當中的短基線密集陣列（the Atacama Compact Array，簡稱 ACA）影像修正用。運用內插和外插的演算技巧來比較與了解影像相位補償修正的有效程度。

Content

List of Figures

List of Tables

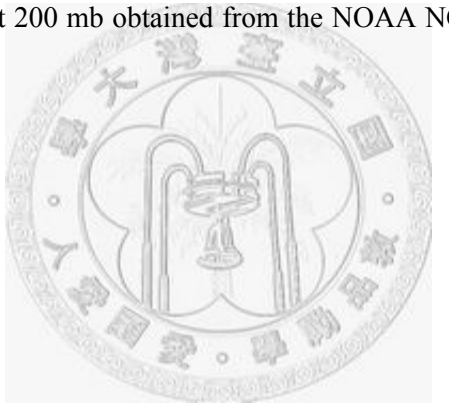

Acknowledgements

I wish to express my heartfelt gratitude to my supervisor Dr. Matsushita, Satoki and Prof. Huang, Keh-Ning for their guidance and generous support with patience during my years as a master student. I am very grateful for the opportunity to join the Institute of Astronomy and Astrophysics in Academia Sinica. Dr. Takakuwa, Shigehisa is greatly appreciated, as was his careful reading of my thesis. I am very fortunate to be indebted to the SMA group in the ASIAA for communications and discussions.

And I thank Dr. Huang, Chun-feng and all the members in R219 in ASIAM for very helpful suggestions. The never-ending encouragement and support from my familly.

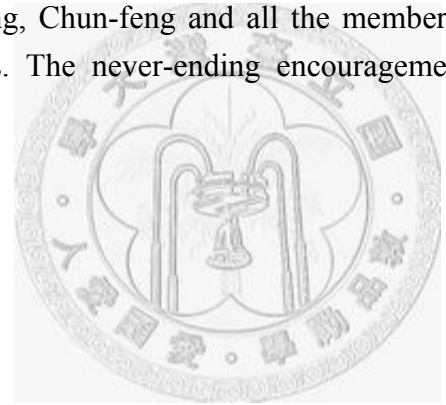

Abstract

Millimeter and submillimeter astronomers pursue science and technology development with ground-based millimeter/submillimeter interferometers through the opaque atmosphere. This waveband provides a unique window on cold dust emission and highly excited lines from molecules and ions. The next generation interferometer at this waveband is the Atacama Large Millimeter and submillimeter Array (ALMA) with the Atacama Compact Array (ACA). The interferometers at this waveband are, however, highly affected by the water vapor induced refraction, which results as phase fluctuations. To reduce the phase fluctuation, we conducted a phase correction scheme using the observing data of the Submillimeter Array (SMA) for the ACA. The phase correction schemes, interpolation and extrapolation, are studied to know how effective these scheme are.

Three simultaneously detected antenna phases form a plane of a wave front, and this phase screen are used for the interpolation and extrapolation. The interpolation scheme can apparently obtain improved results, while the extrapolation scheme often does not.

There are unexpectedly large phase fluctuations showed up only around the 60 meters away from the reference antennas. This can be explained with considering the frozen phase screen.

It may be explained more clearly after more careful investigation of the wind aloft and the temporal and spatial turbulent structure on the summit of Mauna Kea.

Chapter 1
Introduction

Submillimeter and millimeter wavebands are perhaps the last wholly unexplored wavelength frontier because of the technical difficulties and opaqueness of the atmosphere. Here we conducted a scheme to compensate the interferometric phase via SMA observations for the phase correction of the Atacama Compact Array (ACA) in part of the Atacama Large Millimeter and submillimeter Array (ALMA) project.

Astronomers place the millimeter and submillimeter observation wavebands between 30 and 950 GHz with wavelength from 10 mm to 0.3 mm, which are technically difficult due to the sheer complexity of the antenna receivers and to the strong absorption of the atmosphere in such a waveband. They are unique in astronomy containing more than 1000 spectral lines (Carilli et al. 1998) of interstellar and circumstellar molecules as well as the thermal continuum spectrum of cold dust at temperatures of 3-100 K (Taylor et al. 1998). Besides, they promise to yield a new view upon the Universe we live in, almost certainly shedding light upon many of the outstanding questions in modern astronomy. They are the only bands in the electromagnetic spectrum which allow studying cold gas and dust in space. Single dish submillimeter telescopes were built after 1980s. The Submillimeter Array (SMA; Ho et al. 2004) is the world's first dedicated submillimeter interferometer exploring one of astronomy's last frontiers at a site at the summit of Mauna Kea in Hawaii. The aim of the SMA is to use interferometric techniques to observe millimeter and submillimeter wavebands (its wavelength ranges from 0.3 to 1.7 millimeter at frequencies from 180 GHz to 900 GHz) with higher angular resolution.

For a ground-based interferometer operating at millimeter and submillimeter wavelengths, ambient atmospheric water vapor will absorb (block) incoming radio waves. At low elevations, where more water vapor resides, the atmosphere is very opaque at submillimeter wavelengths. The abundant water vapor absorbs a lot of incoming submillimeter light before they can reach the antenna. As a result, observations in the millimeter and submillimeter range are strongly affected by fluctuations in distribution of tropospheric water vapor (Tatarskii 1961). Such variations can cause interferometric image to quiver or to be unstable because the arrival of radio light is affected by the changing index of refraction along its path of

sight through the atmosphere.

Correction of the atmospheric phase fluctuations due to the spatial and temporal variations of the water vapor content in the troposphere is of great importance in radio interferometry, especially in the millimeter and submillimeter wavebands. Even for the observations using the SMA, which is located at the top of Mauna Kea that is one of the best observing sites in the world, phase fluctuations can be seen very often. The water vapor induced phase errors should be removed or calibrated before constructing the interference. Measurements of the water vapor content are very important, but the water vapor is poorly mixed in the atmosphere, and the total column density of the water vapor cannot be accurately sensed from surface meteorological measurements. In addition, higher operating frequency will lead to more phase fluctuations. Several kinds of conventional techniques have been proposed for reducing tropospheric phase noise. They are fast switching phase calibration, paired array phase calibration, radiometric phase calibration, and so on (Carilli and Holdaway 1999).

The ALMA, the largest ground based and astronomical observational facility ever built, is currently under construction in the Chajnantor area in the Atacama Desert in northern Chile. The ALMA is designed to cover the wavelength range from 0.3 mm to 9 mm (almost the same as the SMA) with the ability to provide images at an angular resolution of 0.01 arcsec. The ACA is designed to improve the short baseline coverage of the ALMA, especially for observations of extended and large scale structures at submillimeter wavelength (Fig.1.1).

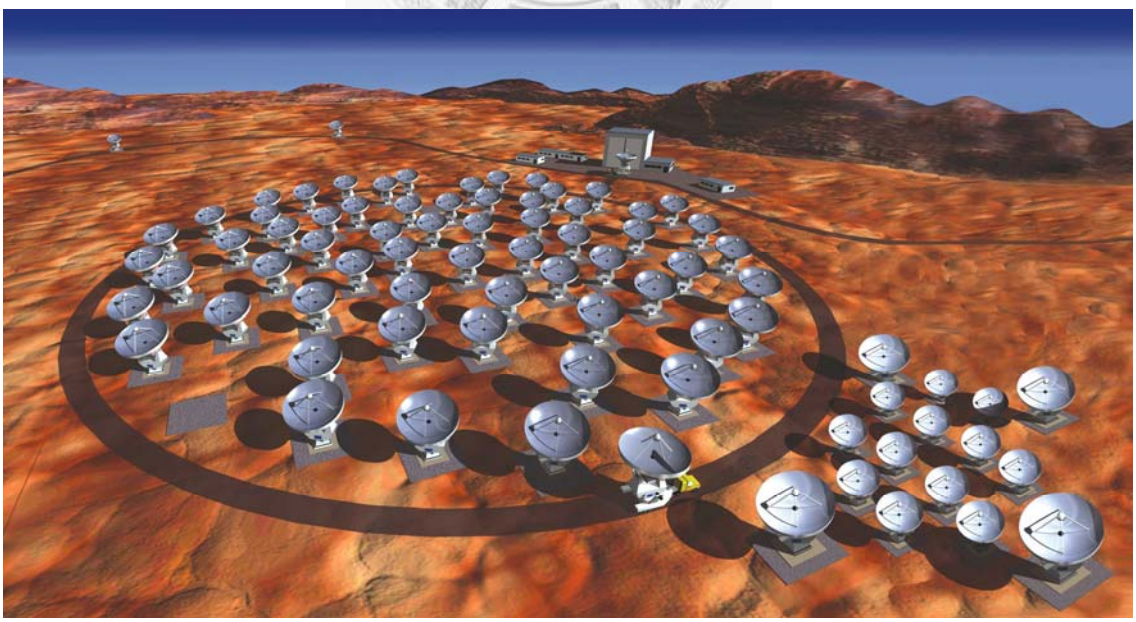

Figure 1.1 Artist's conception of the ALMA antennas in a compact configuration. Image courtesy of NRAO/AUT and ESO. The ACA is at the bottom-right corner of the figure.

Asaki et al. (2005) conducted a series of simulations of a phase calibration scheme for the ACA using water vapor radiometers (WVRs). In the proposed scheme, the WVRs that measure the tropospheric water vapor content are attached to the 12-m antennas at the four corners of the array. The interferometric phase change due to the tropospheric water vapor variations aloft is transferred into the excess path length of the arriving radio waves. The excess path length is fitted to a simple two-dimensional slope using WVR measurements. Then the phases of the antennas inside the reference rectangle can be compensated and calibrated. Note that under a compact configuration, the fast switching phase calibration will not work effectively (Holdaway 2004).

To confirm this simulation study and discuss further, we performed the proposed phase calibration scheme for the ACA using the SMA datasets. Here we present observations with the SMA at 230 GHz, analyze the datasets under the proposed scheme, and discuss the results of the corrected phase variations. Our experiment is to clarify how effectively the proposed compensation scheme works in the conditions of the real atmosphere. We construct a reference triangle composed of three antennas, and make a flat phase plane with observing a point source. The phase of antennas inside the reference triangle can be interpolated, while the phase of antennas outside can be extrapolated. Then we compare the observed phases and the predicted phases of the point source. Standard deviations for the observed and the subtracted phases are compared. Temporal structure functions for the observed and the subtracted phases are used to evaluate how stable the fluctuations are.

Chapter 2
Theory

2.1 Basic Principle of Millimeter and Submillimeter Interferometry

2.1.1 Electromagnetic Waves from Astronomical Sources

Away from our Earth, vast numbers of various astronomical sources emit electromagnetic waves. The electromagnetic waves propagate through space with obeying the well-known Maxwell's equations. Some of the waves travel toward our Earth, and reach to our sensing device—antennas for submillimeter and millimeter astronomy. The arrived waves, or in other words signals, yield electric currents in the antennas, and give us information about the electromagnetic fields at the astronomical sources.

2.1.2 Two-Element Interferometer

To obtain the detailed spatial distributions of the astronomical sources, the size an antenna is needed to be large. However, the size of an antenna cannot be too large due to the technical and budgetary problems. To avoid these problems, interferometry was invented. Much of the early works in interferometric imaging were done by radio astronomers. The signals from two radio antennas were added electronically to produce interference. Later interferometers included a variable delay between one of the antennas and the correlator as shown in Figure 2.1.

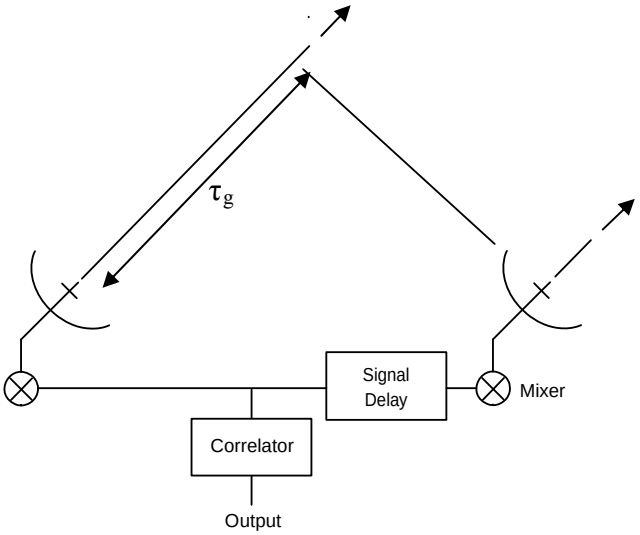

Figure 2.1 The simple diagram of the two-element Michelson interferometer. The path delay τ_g is compensated by the delay circuit.

We define the response of the interferometer as the complex visibility, $V(u,v)$, and the sky brightness distribution as $B(x,y)$. The spatial coherence function can be expressed as follows:

$$V(u,v) = \int B(x,y) e^{i2\pi(ux+vy)} dxdy \,. \tag{2.1}$$

Equation (2.1) demonstrates the Fourier Transform relationship between $B(x,y)$ and $V(u,v)$. Interferometric observations, therefore, measure the Fourier transformed source brightness distribution at a particular spatial frequency due to the limited numbers of antennas. The spatial frequency is given by the baseline vector of two antennas, projected onto the *uv*-plane.

The schematic diagram depicted in Figure 2.2 shows the source plane, the *uv*-plane, and the celestial sphere. The Fourier transform of the source distribution is measured in this *uv*-plane. According to the theory of Fourier transform, a source with an angular extent of x has a largest spatial frequency of u proportional to $1/x$. Thus, if a source exhibits fringes in the spatial frequency of u, the source must have an angular size less than x. If we need to observe an object with a large-scale structure, we need a compact array with short baselines.

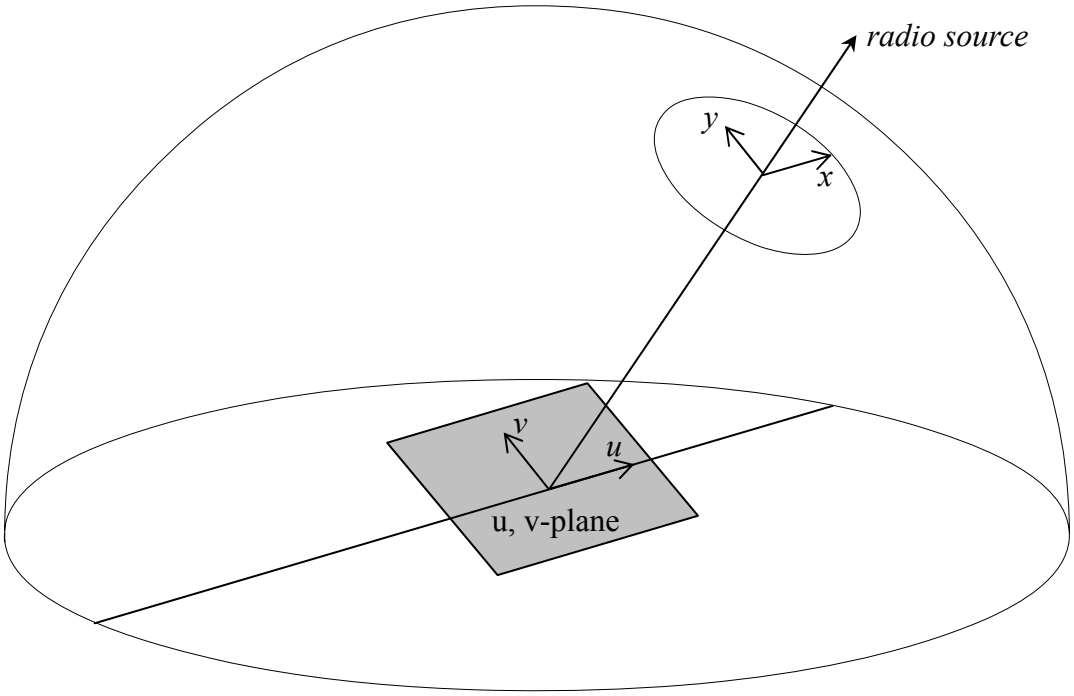

Figure 2.2 The geometric relationship between a radio source and the *uv*-plane, depicted in relation to the celestial sphere. The components of the offsets to the source center is expressed as *x* and *y*.

2.2 Mean Tropospheric Effect on Interferometric Phase

2.2.1 Water Vapor Induces Phase Variation

The neutral media between astronomical sources and our Earth often have profound effects on radiation fields traversing them. Propagation of radio waves through the Earth's neutral atmosphere causes a fluctuation of the phase due to refraction within the medium. These effects can be analyzed in terms of geometric optics. They are the change of the propagating velocity and the deflection of the radio signals.

In the troposphere, which is the lowest layer of the atmosphere, the temperature begins to decrease from the Earth's surface at a lapse rate of 6.5 K km^{-1} until it reaches about 218 K at an altitude of approximately 7 to 11 km. Within the neutral

atmosphere, the propagation of radio waves is most affected by the troposphere. The phase fluctuations in radio interferometers at centimeter, millimeter, and submillimeter wavelengths are caused predominantly by fluctuations in the distribution of water vapor. Uncertainties of water vapor content limit the accuracy of interferometric angular resolution especially at millimeter and submillimeter wavebands. Furthermore, the water vapor is poorly mixed and inhomogeneously distributed in the atmosphere, such as clouds or fog, and the content of the water vapor cannot be accurately sensed from ground-based meteorological measurements.

2.2.2 Excess Path Length and Refractivity

Differences in the refractive index of the atmosphere along the line-of-sight from the different antennas to a radio source cause phase changes (Thompson et al. 2001). Let us consider an electromagnetic wave propagating along the y direction in a uniform dissipative dielectric medium. The wave equation can be represented as

$$\mathbf{E}(y,t) = \mathbf{E}_0 e^{i(kny - 2\pi\nu t)}, \tag{2.2}$$

where $\mathbf{E}_0$ is the electric field amplitude, n describes the complex index of refraction, and k is the propagation constant in free space, equal to $2\pi\nu/c$, where c is the speed of light. Assume that the effect of the difference in physical length between the actual wave path and the straight-line path is negligible and the source is in the far-field of the antennas, where the antenna primary beam pattern is essentially independent of the distance from the source.

The difference between the time to penetrate through a medium with index of refraction $n(y)$ and the time required to traverse the same distance in free space is

$$\Delta t = \frac{1}{c}\int (n-1)dy\,. \tag{2.3}$$

In most radio astronomical studies, the excess path length L is defined as $c\Delta t$,

$$L = 10^{-6}\int N(y)dy\,, \tag{2.4}$$

where N is the refractivity, defined by $N = 10^6(n-1)$. The excess path length is used extensively in millimeter radio astronomy.

The refractivity of moist air can be approximated by the Smith-Weintraub equation (Smith 1953)

$$N = 77.6\frac{p_D}{T} + 64.8\frac{p_V}{T} + 3.776\times 10^5\frac{p_V}{T^2}, \tag{2.5}$$

where T is the temperature in Kelvin, p_{D} and p_{V} are the partial pressures of the dry air and the water vapor in millibars (1 mb = 1 hPa = 100 N/m^2), respectively.

According to the ideal gas law, the refractivity can be written in terms of gas density

$$p = \frac{\rho RT}{M}, \tag{2.6}$$

where p and ρ are the partial pressure and mass density of the constituent gas, R is the universal gas constant, and M is the molecular mass. The air is a mixture of the dry and wet components. The equation of state of these two components are $p_{\mathrm{D}} = \rho_{\mathrm{D}} RT / M_{\mathrm{D}}$ and $p_{\mathrm{V}} = \rho_{\mathrm{V}} RT / M_{\mathrm{V}}$, where ρ_{D} and ρ_{V} are the mass densities of the dry air and water vapor, respectively. The molecular mass for the dry air in the troposphere is M_{D} = 28.96 g mol^{-1} and that for water vapor is M_{v} = 18.02 g mol^{-1}.

According to the Dalton's law, the total pressure p is the sum of all the partial pressures, and the total density ρ_T is the sum of the densities of dry air and water vapor. The total pressure p can therefore be replaced by ρ and written as

$$p = \frac{\rho_T RT}{M_T},$$

where

$$M_T = \left[\frac{1}{M_D}\frac{\rho_D}{\rho_T} + \frac{1}{M_V}\frac{\rho_V}{\rho_T}\right]^{-1}. \tag{2.7}$$

Substituting Eq.(2.6) and the equation $\rho_D = \rho_T - \rho_V$ into Eq.(2.5) yields

$$N = 0.2228\rho_T + 0.076\rho_V + 1742\frac{\rho_V}{T}, \tag{2.8}$$

where ρ_T and ρ_V are in g m^{-3}. Since the second term on the right-hand side of Eq.(2.8) is small with respect to the third term, it can be combined with the third term under the condition of T = 280 K,

$$N = 0.2228\rho_T + \frac{0.076\times 280\rho_V}{T} + 1742\frac{\rho_V}{T} \approx 0.2228\rho_T + 1764\frac{\rho_V}{T} = N_D + N_V . \tag{2.9}$$

The refractivity can be divided into the contribution of the dry and wet refractivities, which are defined as N_D and N_V, respectively.

The equation below describes an air parcel in static equilibrium between pressure and gravity

$$\frac{dp}{dh} = -\rho_T \mathrm{g}, \tag{2.10}$$

where g is the acceleration due to gravity, approximately equal to 980 cm s^{-2}, and h is the height above the Earth's surface. The equation of hydrostatic equilibrium for the atmosphere can be applied to a high degree of accuracy (Humphreys 1940). Using the ideal gas law, Eq(2.6), we integrate Eq.(2.10) with assuming an isothermal atmosphere and a constant mixing ratio. The solution can be written as $\rho_T(h) = \rho_T(0)e^{-Mgh/RT}$. This is an exponential function with a scale height of RT/Mg = 8.5 km for 290 K, which is close to the observed scale height. The surface pressure can be obtained by integrating Eq.(2.10) as follows, assuming g to be constant with height:

$$P_0 = g\int_0^\infty \rho_T(h)dh . \tag{2.11}$$

From Eq.(2.4), (2.9), and (2.11), the dry excess path length in zenith direction is

$$L_D = 10^{-6}\int_0^\infty N_D dh = \left(\frac{77.6R}{\mathrm{gM_D}}\right)P_0 = 0.228P_0 . \tag{2.12}$$

The excess path length in centimeter due to the dry component of refractivity (L_D)

does not depend on the height distribution of total density or temperature, but only on the surface pressure P_0, under the conditions of hydrostatic equilibrium in the assumed isothermal atmosphere.

Water vapor is not well mixed in the atmosphere and therefore is not well correlated with ground-based meteorological parameters (Reber and Swope 1972). On average, water vapor density has an exponential distribution

$$\rho_V(h) = \rho_V(0)e^{-M_V gh/RT} \tag{2.13}$$

with a scale height of 2 km. From Eq.(2.6), the relation between the partial pressure and the density of water vapor can be expressed as

$$\rho_V = \frac{M_V p_V}{RT}, \tag{2.14}$$

where M_v = 18.02 g mol^{-1} and R = 8.314 J mol^{-1} K^{-1}, thus $\frac{M_V}{R} \approx 217$ and therefore

$$\rho_V = \frac{217 p_V}{T} \quad [\text{g m}^{-3}]. \tag{2.15}$$

The partial pressure of water vapor, p_{VS}, for saturated air at temperature T, can be obtained from the Clausius-Clapeyron equation (Hess 1959) to an accuracy of better than 1% within the temperature range 240-310 K by the formula

$$p_{VS} = 6.11\left(\frac{T}{273}\right)^{-5.3} e^{25.2(T-273)/T} \quad [\text{mb}]. \tag{2.16}$$

Note that p_V/p_{VS} is the relative humidity (Crane 1976). Eq.(2.16) represents the partial pressure of water vapor at temperature T. Compared to the other gases in the air, water may easily condensate. The water vapor pressure is in general very low compared to the air pressure in a mixture. Common values for the vapor pressure are between 5 to 30 mb. The component of the path length resulting primarily from water vapor is

$$L_V = 1763 \times 10^{-6} \int_0^\infty \frac{\rho_V(h)}{T(h)} dh . \tag{2.17}$$

We assume that the atmosphere is isothermal and that p_V decreases exponentially with a scale height of 2 km,

$$p_V(h) = p_V(0) e^{-M_V g h / RT} \tag{2.18}$$

and

$$\frac{RT}{Mg} = 2 \quad \text{[km]},$$

then from Eqs.(2.15) and (2.17)

$$L_V = 7.6 \times 10^4 \frac{p_{V0}}{T^2} \quad \text{[cm]}, \tag{2.19}$$

where p_{V0} is the partial pressure of water vapor at the surface of the earth. We denote the precipitable water vapor density as

$$w = \frac{1}{\rho_W} \int_0^\infty \rho_V(h) dh , \tag{2.20}$$

where ρ_W is the density of water, 10^6 g m^{-3}. Suppose that the atmosphere is isothermal at 280 K in Eq.(2.17)

$$L_V \approx 6.3 w . \tag{2.21}$$

This widely used formula is an excellent approximation for frequencies below 100 GHz. In the operating wavebands above 100 GHz, the ratio L_V/w can increase from 6.3 to about 8 (Fig.2.3).

The total zenith excess path length through the atmosphere is $L \approx L_D + L_V$ in centimeter, which from Eqs.(2.12) and (2.21) is

$$L \approx 0.228 P_0 + 6.3 w , \tag{2.22}$$

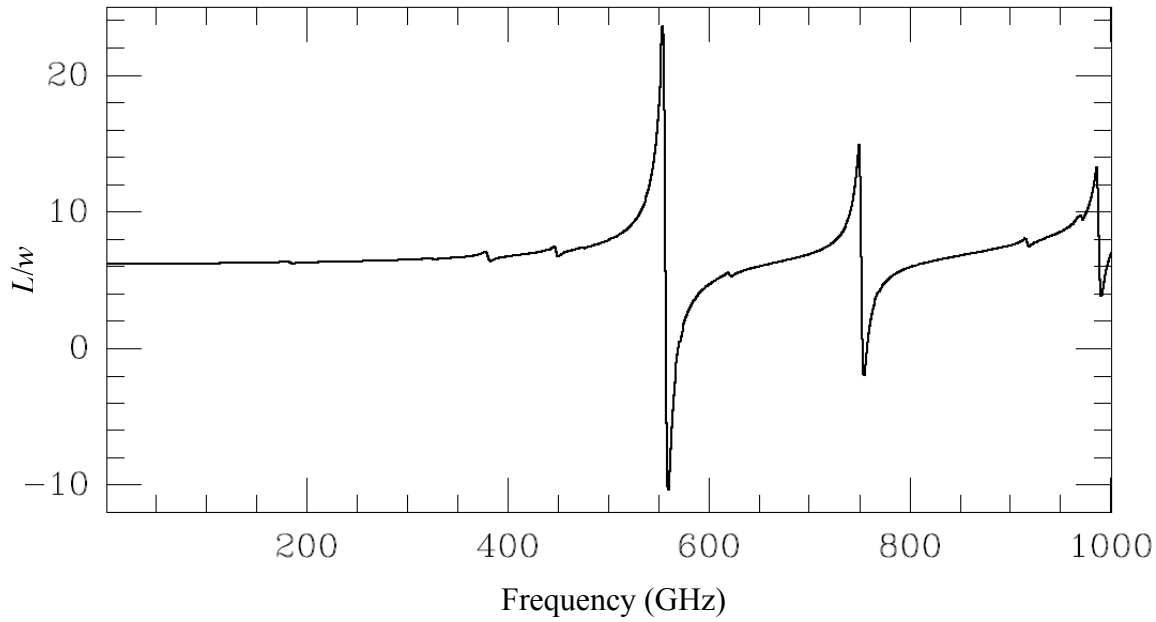

Figure 2.3 The excess path length due to water vapor per unit column density versus frequency, from formulas by Liebe (1989) (Sutton and Hueckstaedt 1996).

where P_0 is in millibars, and w is in centimeters. Equation (2.22) shows that the excess path length L depends on the meteorological condition and is reasonable for estimation purposes. However, it is usually not accurate enough to predict the path length of a wavelength at millimeter and at submillimeter wavelengths. Table 3.1 shows two different meteorological conditions for estimation purposes. More precipitable water vapor can cause longer excess path length.

Table 2.1 Two different physical conditions for estimation purposes. More precipitable water vapor density leads to longer excess path length due to water vapor.

Meteorological Parameter	Case I	Case II
Temperature (K)	303	258
Relative Humidity (%)	80	50
P_{V0}(mb)	34	1.0
ρ_{V0}(g/m^3)	24	0.8
w (cm)	4.9	0.15
L_V(cm)	28	1.1

2.3 Phase Change in the Atmosphere

We use a simple model (McKinnon 1988) to present the phase change in the process of radio wave propagation in the neutral atmosphere, troposphere. Let the atmosphere above the interferometer be flat, as opposed to be curved in the reality, with a uniform thickness h and the water vapor layer above one antenna have thickness w_m and the water vapor layer above the other antenna have thickness w_n. To carry out the radio wave propagating through the atmosphere, we use the Equation (2.2)

$$\mathbf{E}(y,t) = \mathbf{E}_0 e^{i(kny - 2\pi\nu t)}, \tag{2.23}$$

where k is in general complex ($k = 2\pi\nu/c$). For waves propagating along the y direction in a dissipative medium (non-dispersive), which is a poor conductor (Jackson 1998), k can be expressed as

$$k \approx \frac{2\pi\nu}{c}\sqrt{\mu\varepsilon} + i4\pi^2\sigma\frac{\nu}{c}\sqrt{\frac{\mu}{\varepsilon}}. \tag{2.24}$$

Substituting this term for k into Eq.(2.23), the equation can be rewritten as follows

$$\mathbf{E}(y,t) = \mathbf{E}_0 e^{-4\pi^2\sigma y\frac{\nu}{c}\sqrt{\frac{\mu}{\varepsilon}}} e^{i\frac{2\pi\nu}{c}(y\sqrt{\mu\varepsilon} - ct)}. \tag{2.25}$$

The phase of the propagating wave in the equation above is

$$\phi = \frac{2\pi\nu}{c}ny - 2\pi\nu t, \tag{2.26}$$

since the medium index of the refraction is $n = \sqrt{\mu\varepsilon}$.

After the wave propagates through atmosphere, the phase of the radio wave arriving at each antenna becomes

$$\phi_m = \frac{2\pi\nu}{c}\left[(h - w_m) + nw_m\right] - 2\pi\nu t, \tag{2.27}$$

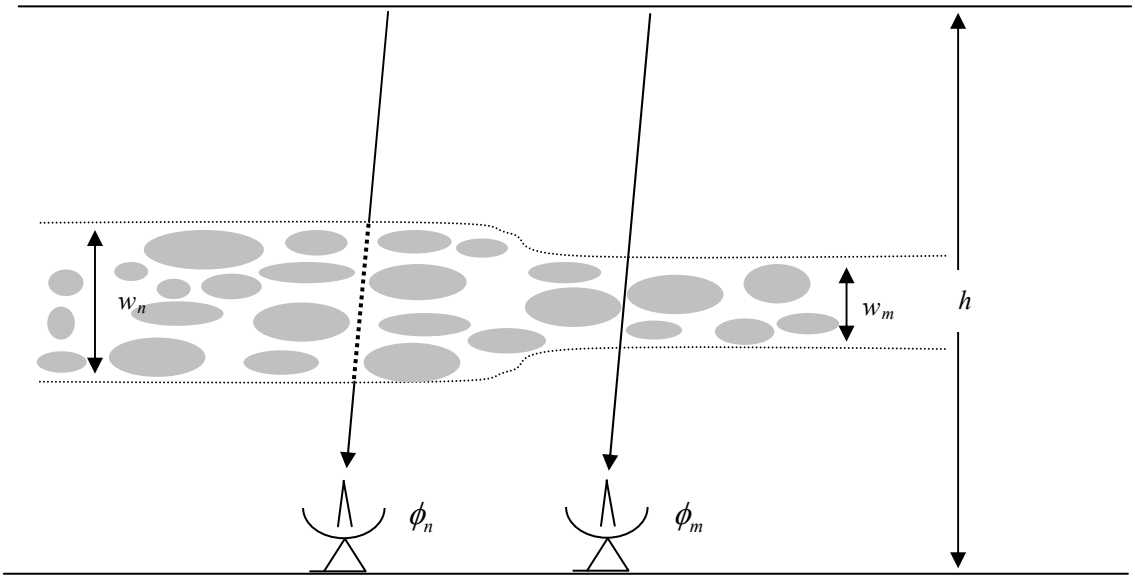

Figure 2.4 Schematic diagram of water vapor induced excess path length and phase difference between two connected element antennas. It shows that the interferometric phases change more as radio wave propagating through more water vapor fluctuations.

$$\phi_n = \frac{2\pi\nu}{c}\left[(h - w_n) + nw_n\right] - 2\pi\nu t, \tag{2.28}$$

where n is now the refractive index of water vapor and the refractive index of air is assumed to be unitary, and ϕ_m and ϕ_n are the two phases for each antenna (Fig.2.4). The phase delay between the two antennas is therefore

$$\Delta\phi = \phi_n - \phi_m = \frac{2\pi\nu}{c}\left[n(w_n - w_m) - (w_n - w_m)\right]. \tag{2.28}$$

If D is the difference in signal path length above the two connected antennas, then $w = w_n - w_m$ and

$$\Delta\phi = 2\pi\nu w(n-1)/c = 2\pi(n-1)\times\frac{w}{\lambda} = 2\pi\times10^{-6}\times N\times\frac{w}{\lambda}, \tag{2.29}$$

where we have introduced the refractivity N, defined by $N = 10^6(n-1)$. In terms of excess path length L, the equation can be expressed as

Table 2.2 Theoretical calculation at 230 GHz of the two days on the summit of Mauna Kea.

Time of Observation	PWV (mm)	Phase Difference (degree)
Thu Aug 26, 2004 (10 HST) MKWC	1.0	30°
Tue Sep 07, 2004 (17 HST) MKWC	5.0	152°

$$L = \lambda \times \frac{\Delta\phi}{2\pi} = 10^{-6} \times N \times w. \tag{2.30}$$

The equation above illustrates the effect of the atmosphere on phase delay. The real atmosphere is turbulent, and water vapor is not uniformly distributed in the troposphere. According to the Equation (2.29), the phase delay increases with the water vapor content and the frequency of the incident radio wave. As our operating frequency is getting higher, water vapor for phase fluctuations affects more. In the case of the SMA observing at 230 GHz (wavelength = 1.3 mm), the difference of the phase under different weather conditions can be roughly calculated as listed in Table 3.2. Therefore it is necessary to develop a suitable strategy to compensate the tropospheric phase fluctuations due to water vapor for millimeter and submillimeter interferometers with higher and higher frequencies.

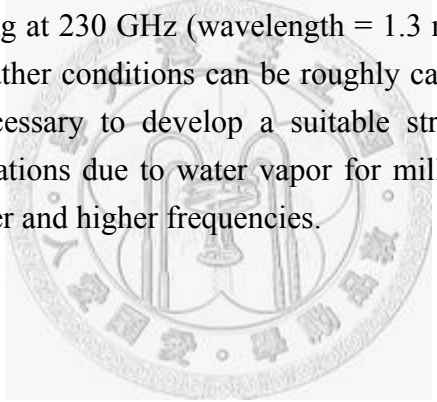

Chapter 3
Measurements and Data Reduction

The purpose of the experiment is to investigate the proposed phase compensation method for the ACA using the SMA on Mauna Kea. The reasons of using the SMA for this experiment are that the SMA is an interferometer operating at submillimeter wavelengths, which is the same as the ACA, and that the antenna configuration of the array is applicable for this experiment. The ACA uses WVRs for the phase compensation, but for this experiment using the SMA, we observed strong point sources to measure the phase directly.

3.1 Measurements

3.1.1 The Submillimeter Array (SMA)

The SMA has been constructed at the foot of Pu'u Poli'ahu at 4080 m above sea level at the summit of Mauna Kea, Hawaii, U.S.A. (Fig. 3.1) as a collaborative project of between the Smithsonian Astrophysical Observatory (SAO) and the Academia Sinica Institute of Astronomy & Astrophysics (ASIAA). Figure 3.2 shows all antennas of the SMA. Eight 6-m radio antennas comprise the array with currently working receiver bands at 230, 345, and 690 GHz. Each element can observe with two receivers simultaneously, with two sidebands and a 2 GHz bandwidth each. The array will have 8 receiver bands covering the frequency range of 180-900 GHz. The SMA can achieve angular resolutions down to about 0.5 arcsecond at 200 GHz and, eventually at highest, 0.1 arcsecond at 850 GHz, providing at least 60 times sharper images than those the existing submillimeter-wave single-dish telescopes (such as the Caltech Submillimeter Observatory [CSO], the James Clerk Maxwell Telescope [JCMT] and the Atacama Submillimeter Telescope Experiment [ASTE]) can provide. Observations conducted on the SMA are to study stars and planets formations, stellar evolutions, the center of our Galaxy and nearby galaxies, early universe, and so on.

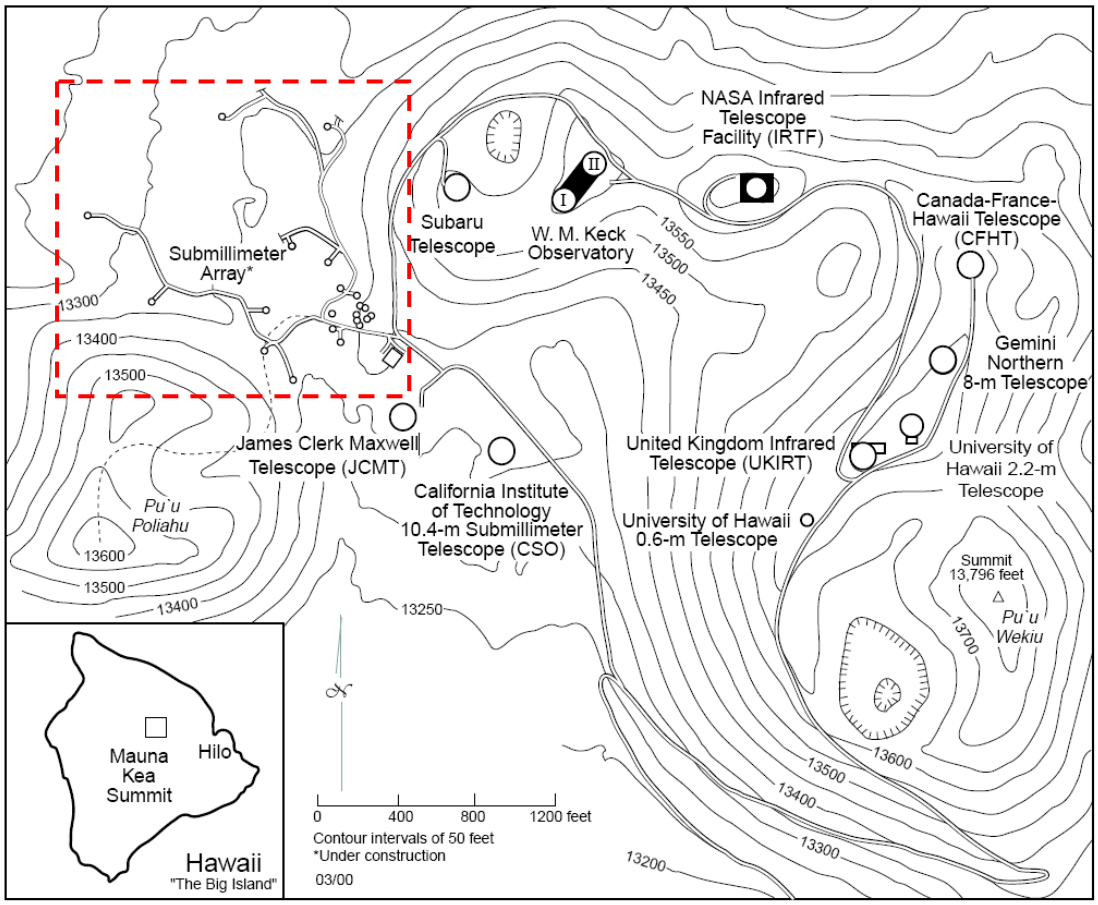

Figure 3.1 Locations of summit facilities of the Mauna Kea observatories. The SMA is located in the red dotted rectangle (courtesy of Institute for Astronomy of University of Hawaii).

Figure 3.2 All 8 antennas of the SMA observing during the SMA dedication, November 22nd 2004 (Ho et al. 2004)

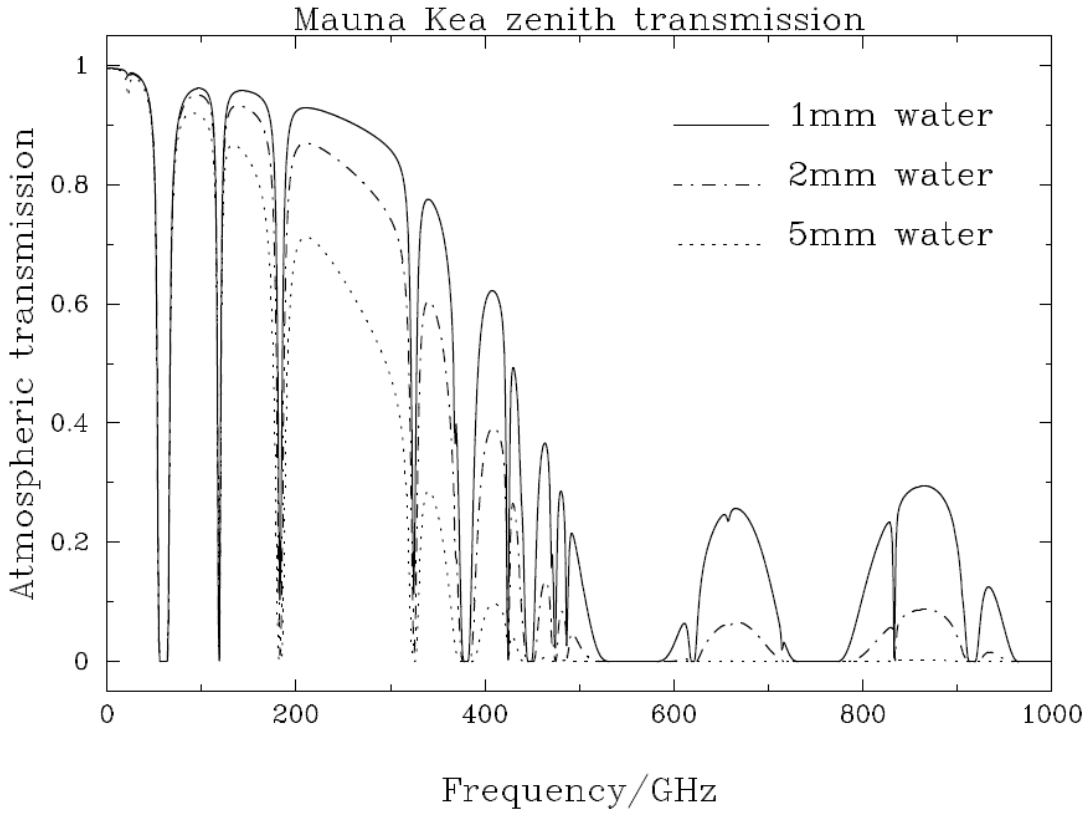

Figure 3.3 Three different precipitable water vapor (PWV), 1 mm, 2 mm, and 5 mm, with different atmospheric transmission (Wiedner 1998).

The emissions at submillimeter and millimeter wavelengths from astronomical sources are partially absorbed by water vapor in the Earth's atmosphere. At sea level, little submillimeter radiation reaches the Earth's surface, and therefore ground-based astronomical observations at submillimeter and millimeter wavebands are very difficult. By building the SMA on a high and dry site, the radiation can be detected and measured through the atmospheric window (Wiedner 1998). The atmospheric transmission spectrum on Mauna Kea is in Figure 3.3.

3.1.2 Measurements

The measurements were carried out on August 26, 2004 and September 7, 2004 using all eight antennas. The antenna configuration is depicted in Figure 3.4. The shortest and longest baselines are 11.60038 meters (antenna 1 to antenna 8) and

179.2118 meters (antenna 4 to antenna 6), respectively. The measurements were performed at 240.0 GHz for the August 26, 2004 measurement and 230.5 GHz for the September 7, 2004 measurement. The data were stored in the SMA archive directories 040826_01:23:23/ and 040907_05:22:09/. Hereafter we call the former dataset as “040826” and the latter “040907”. We observed B1921-293 (J1924-291) in both days for 1.1567 and 0.469 hours, respectively, with the integration time for one data point of 5.16 seconds.

B1921-293 (OV-236) is a southern bright quasar with a 17.5 V-magnitude. At a redshift of 0.352 (Wills and Wills 1981), B1921−293 is one of the closest members of its class. It is one of the strongest and the compact extragalactic radio source known, which makes it a prime candidate for high-resolution VLBI observations. B1921-293, together with 3C273B and 3C279, is currently among the brightest extragalactic sources in the sky at millimeter wavelengths (Tornikoski et al, 1996). The flux at 230 GHz around our observation periods was about 6 Jy. We summarize the basic information of B1921-293 in Table 3.1.

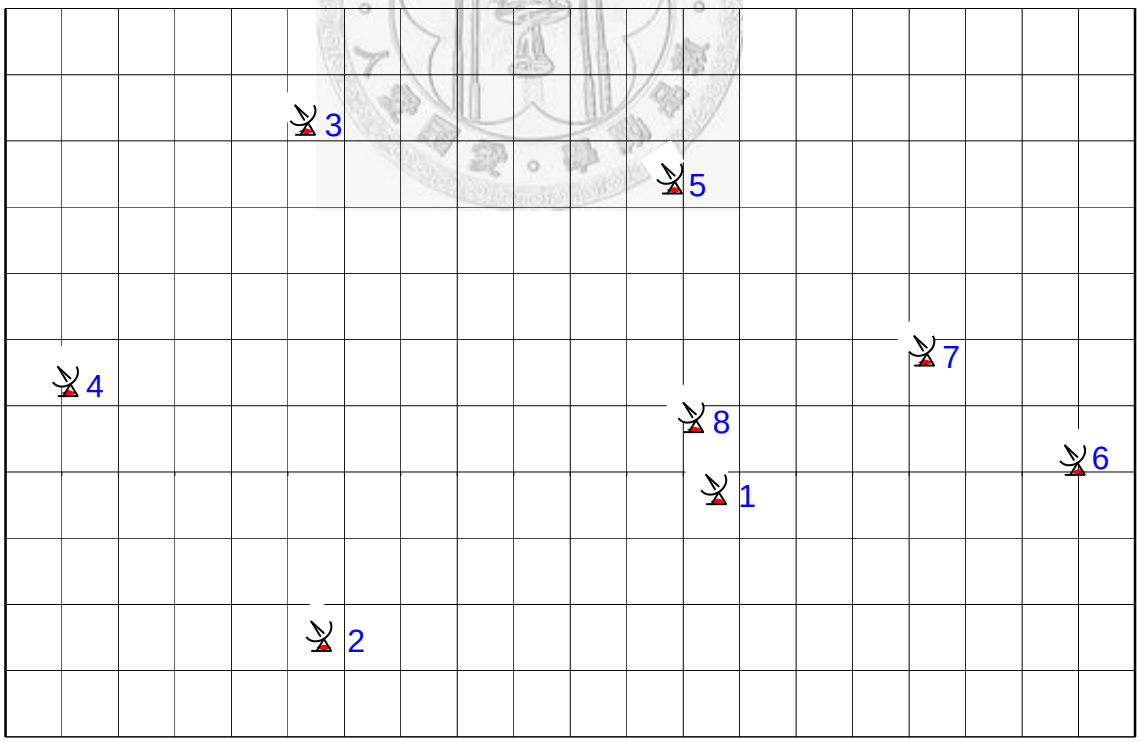

Figure 3.4 Configuration of all eight antennas of the observation for the data reduction, antenna 1 to antenna 8. The length of each side of the rectangle is 10 meters.

Table 3.1 Profile of B1921-293.

Name	other name	right ascension (J2000)	declination (J2000)	230GHz flux density	optical ID	redshift
B1921-293	J1924-291, OV-236	19 h 24 m 51.0559 s	-29°14′ 30.120"	～6 Jy	quasar	0.352

3.2 Data Reduction

3.2.1 Calibration

We reduced the data using the OVRO software MIR adopted for the SMA. The observed target B1921-293 is assumed to be a point source. The data were calibrated based on the antenna-base calibration. We confirmed that all the results did not change with the reference antennas in the antenna-base calibration. Note that since the geometrical (baseline) delay is taken into account at the correlation process (at the SMA backend), we do not need to consider the effect of the antenna altitude.

3.2.2 Construction of Phase Screen

Consider a reference triangle composed of three antennas. A plane of phase or phase screen through these three antennas can be constructed at each integration (data point). We therefore compute the function of this phase screen at each integration using antennas located at the outer periphery of the antenna configuration as reference antennas. There are always several antennas inside and/or outside this reference triangle (Fig. 3.5). Using the phase screens, interpolations and extrapolations are conducted to predict the phase at each antenna position inside or outside the reference antennas, respectively. We then compare the observed phases with our interpolated and extrapolated phases.

We have seven different configurations of reference triangles to interpolate and extrapolate our phases of antennas inside and outside the triangle, respectively. The configurations of all reference triangles we calculated are summarized in Table 3.3.

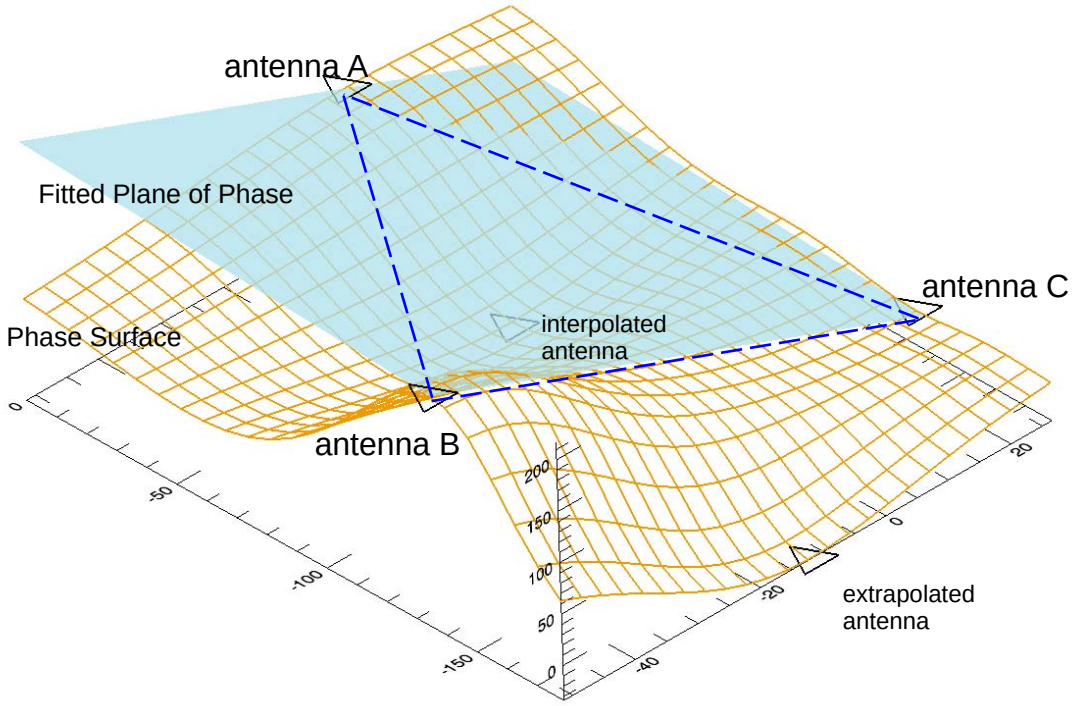

Figure 3.5 Schematic diagram for the proposed plane of phase for interpolations and extrapolations.

Table 3.2 Configurations of reference triangles and the interpolate and extrapolate antennas inside and outside the triangle. The cross in this table means no antenna is inside the reference triangle to do interpolation under that configuration.

Configurations	Datasets			
	040826		040907	
Reference Antennas	Interpolation Antenna(s)	Extrapolation Antennas	Interpolation Antenna(s)	Extrapolation Antennas
[2, 3, 6]	1, 8	4, 5, 7	1,	4, 5, 7
[2, 4, 5]	×	1, 3, 6, 7, 8	×	1, 3, 6, 7
[2, 4, 6]	1, 8	3, 5, 7	1	3, 5, 7
[2, 4, 7]	1, 8	3, 5, 6	1	3, 5, 6
[2, 5, 6]	1, 7, 8	3, 4	1, 7	3, 4
[3, 4, 6]	8	1, 2, 5, 7	×	1, 2, 5, 7
[4, 5, 6]	8	1, 2, 3, 7	×	1, 2, 3, 7

Chapter 4
Results

4.1 Comparisons between Observed, Interpolated, Extrapolated, and Residual Phase Fluctuations

First, we show the phase fluctuation plots of observed data after the antenna-base gain calibration, and the interpolated or extrapolated data estimated from the reference triangle for each antenna in Figure 4.1 and 4.2. Figure 4.1 is the plots for the dataset 040826 with the antenna-base gain calibration referring the antenna 2, and with the reference triangle [2, 3, 6] for the interpolation/extrapolation of the phase. Figure 4.2 is the plots for the dataset 040907 with the antenna-based gain calibration referring the antenna 2, and with the reference triangle [2, 3, 6] for the interpolation/extrapolation of the phase. We overplotted the subtracted (residual) phase fluctuation plots in the same figures, which are calculated as follows:

[subtracted(residual) phase] = [observed antenna-base gain calibrated phase]

$$-[\text{interpolated or extrapolated phase}]. \qquad (4.1)$$

The subtracted phase tells us how much difference between the observed and our estimated interpolated or extrapolated phase is, namely how effective our phase correction is. In these figures, the plotted curve in green, blue, and red are the observed phases, interpolated or extrapolated phases and residual (subtracted) phases, respectively.

To evaluate the effectiveness of the phase correction quantitatively, we calculate the standard deviation of our observed, interpolated/extrapolated, and subtracted phase fluctuations, and shown in Figure 4.1 and 4.2. It appears that the interpolations lead to a smaller standard deviation of residual phases, while the extrapolations do not always improve the phase fluctuation.

Phase correction can not work effectively with too large phase fluctuations in either

interpolation or extrapolation. We find out that the main reason of this failure is because of the 2π ambiguity of the phases. The interferometer can measure the phase only within ±π, so if the phase fluctuates largely, the phases wrap within ±π, and it is difficult to recover the real phase fluctuations larger than ±π.

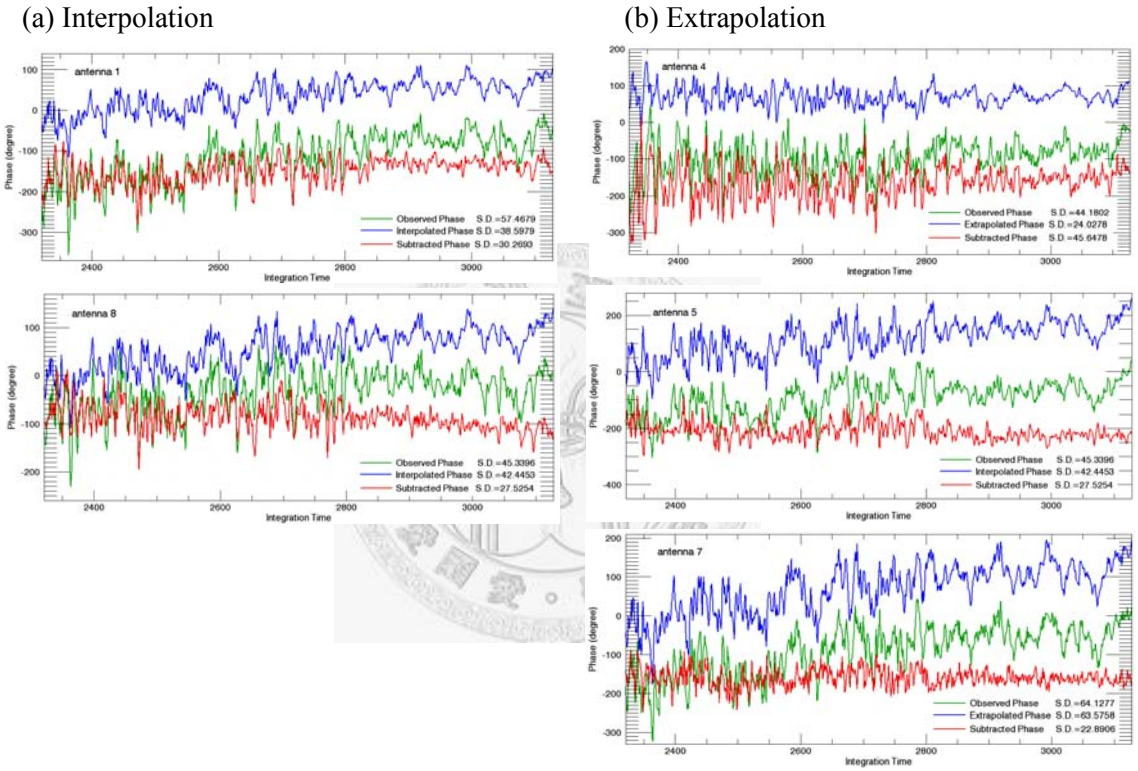

Figure 4.1 The time series plots of the phase from dataset 040826 between the integration number 2321-3128. The green curves show the observed antenna-base gain calibrated data, the blue curves show the interpolated or extrapolated data, and the red curves trace the subtracted data between the observed and modeled (interpolated/extrapolated) phases. S.D. means the standard deviation values for phase fluctuation over the integration time of the observation. The interpolated calculations always have more satisfied results, while the extrapolation calculations do not always have. (a) The interpolation results of the reference triangle [2, 3, 6] for the antennas 1 and 8. (b) The extrapolation results of the reference triangle [2, 3, 6] for the antennas 4, 5, and 7.

(a) Interpolation (b) Extrapolation

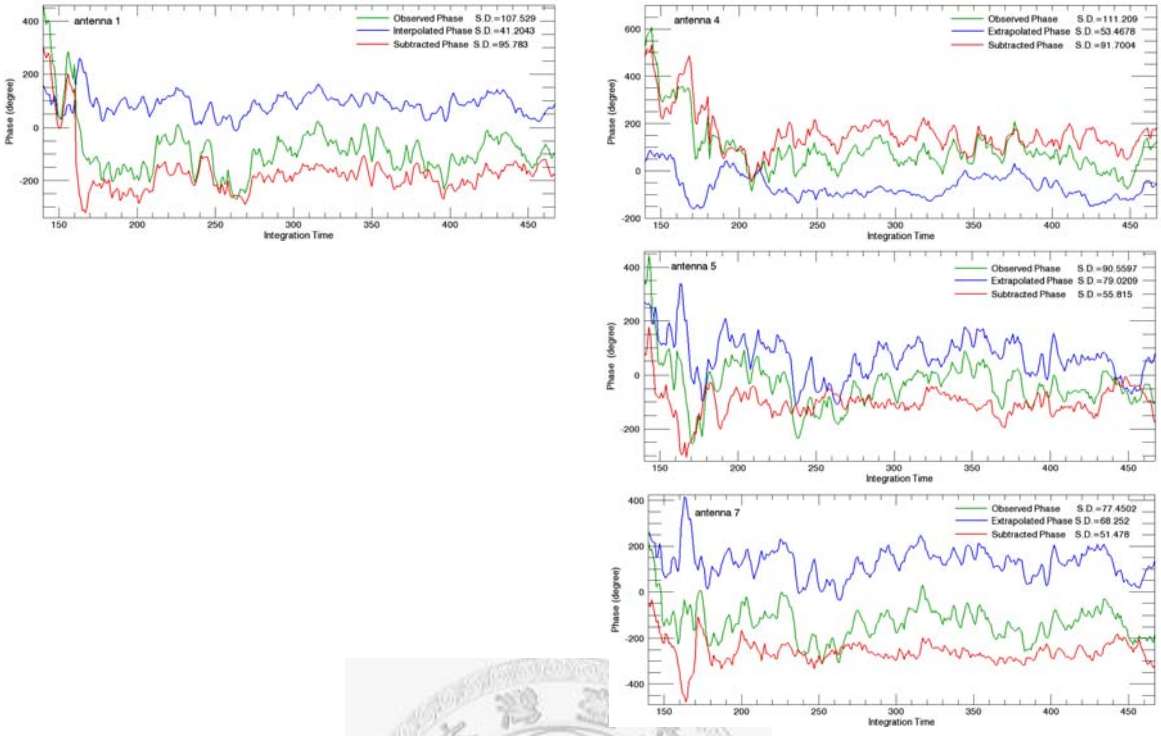

Figure 4.2 The time series plots of the phase from dataset 040907 between the integration number 140-467. Other information is the same as in Figure 6.2. (a) The interpolation results of the reference triangle [2, 3, 6] for the antenna 1. (b) The extrapolation results of the reference triangle [2, 3, 6] for the antennas 4, 5, and 7.

It is interesting to note that observed phases of dataset 040826 are more stable than dataset 040907, and the former one have more satisfied phase correction results. In addition, even within one dataset, phase fluctuation and the degree of phase correction changes drastically. For example, in the dataset 040826, the phase fluctuation and the subtracted phase changes a lot between the integration 2321-2799 and 2800-3128; the standard deviation of phase fluctuation improved a bit for the former case, but improved a lot for the latter case (Fig.4.1). Hereafter we separate each dataset into two integrations and they are shown in Table 4.1. We divided our two datasets into early and later parts. The foreparts of '040826' and '040907' are the integration numbers of 2321-2799 and 140-199, which have larger variations on phase than the later parts of 2800-3128 and 200-467.

Table 4.1 The two datasets are divided via their observed phase variations.

Integration Period	040826	040907
Early Part	2321-2799	140-199
Later Part	2800-3128	200-467

4.2 Re-Define the Phase: Phase Refers to the Center of the Reference Triangle

The improvement of the phase, however, depends on the reference antenna of the antenna-based gain calibration. If the interpolated antenna is close to the reference antenna, the improvement of the phase is small, but if the interpolated antenna is far in spatial distance from the reference antenna, the improvement of the phase is large. In addition, the final results, namely the residual phase fluctuations, do not change with the reference antenna. In Figure 4.3, we show examples of observed and subtracted phases for different reference antennas. As can be seen, in case of the interpolation scheme (Fig. 4.3a) subtracted phases improve in all the three reference antenna cases, but the degree of improvements depends on the reference antennas. In case of the extrapolation scheme (Fig. 4.3b), on the other hand, subtracted phases improve in some reference antenna cases, but some do not.

To evaluate the effectiveness of the phase correction more quantitatively, we re-define the phase to that refers to the center of the reference triangle. In Figure 4.4, we show the schematic diagram of the relations. First, we define ρ as the distance from the center of the reference triangle to our interpolated/extrapolated antennas. The centroid coordinate of the reference triangle is assigned as the center of the reference triangle C. Second, we define the phase reference at the center of the reference triangle. This is because, as mentioned above, the phase derived using antenna-base phase calibration depends on the reference antenna, and therefore difficult to evaluate the improvement of the phase due to the correction.

(a) Interpolation (b) Extrapolation

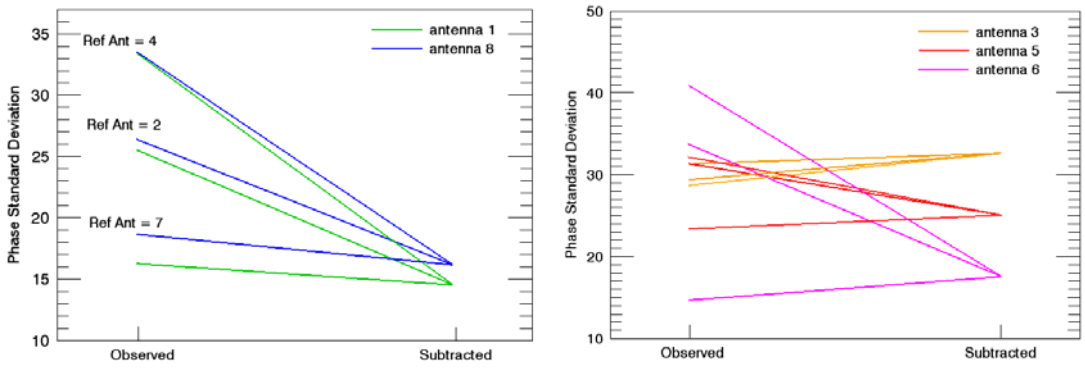

Figure 4.3 Data calibrated with different reference antennas have different observed phase standard deviation, but they all have identical standard deviations for the subtracted phase. (a) The interpolation of antennas 1 and 8 in the reference triangle [2, 4, 7] through integration 2800-3128. (b) The extrapolation of antennas 3, 5 and 6 in the reference triangle [2, 4, 7] through integration 2800-3128.

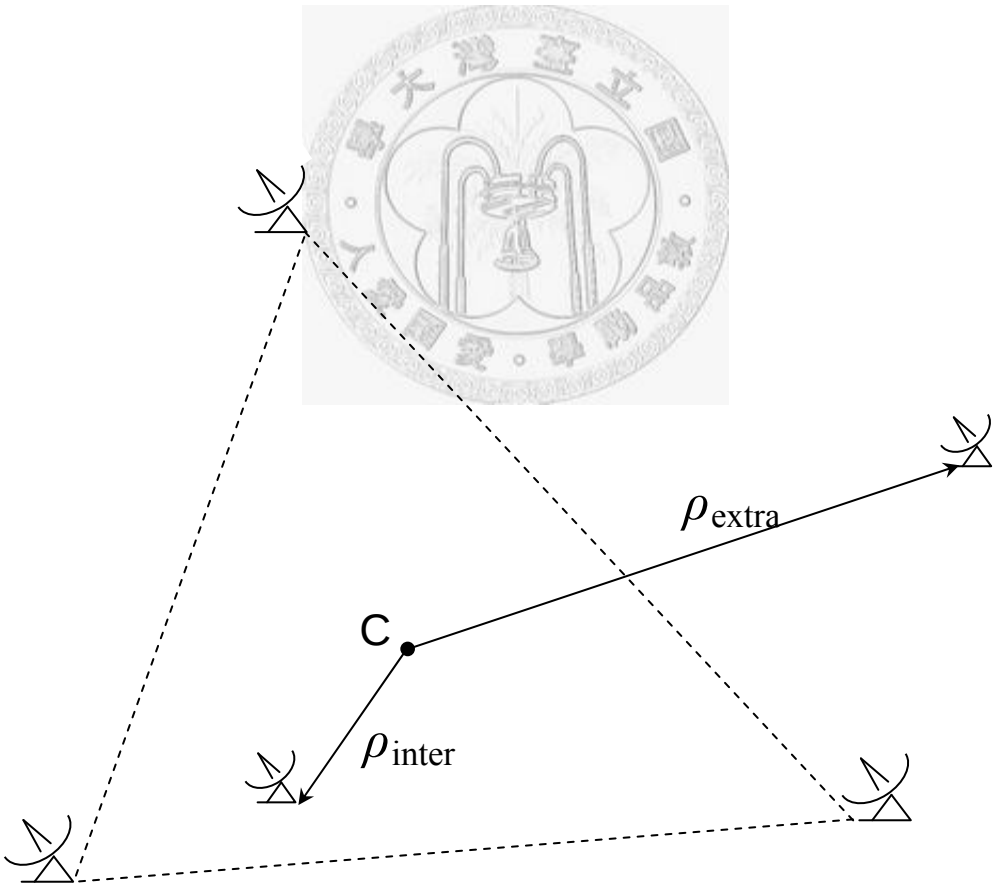

Figure 4.4 The denoted spatial length ρ are the distance from the center of the reference array C to the interpolated/extrapolated antennas. The subscript "inter" and "extra" are corresponding to the distance of the interpolated and extrapolated antennas from C.

(a) Observed Phase (b) Real Phase

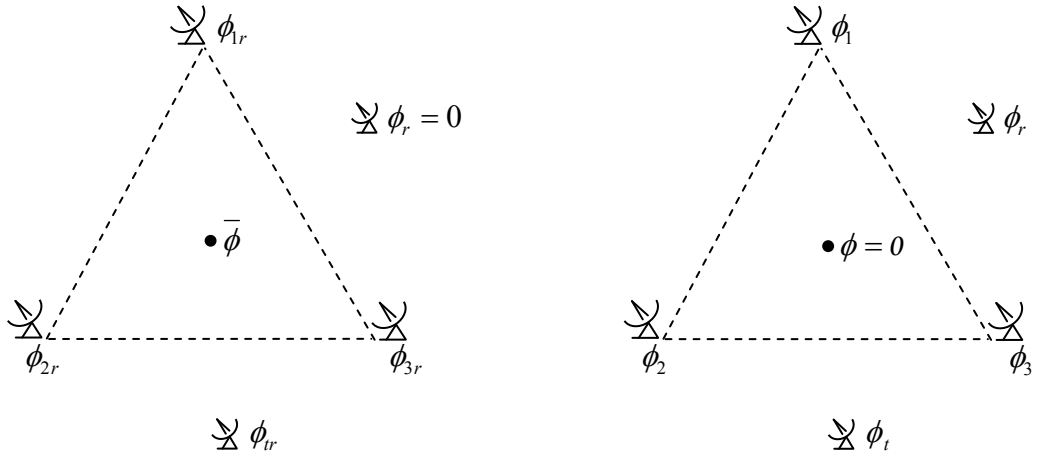

Figure 4.5 The simple diagram of the phase conversion from (a) the observed phase to (b) the real phase. The three antennas 1, 2, and 3 are located at the corner of the triangle configuration. The reference antenna for the antenna-base phase calibration, ***r***, and the target antenna for correcting the phase, ***t***, are also shown in the plots.

Consider a reference triangle composed of three antennas and the detected phases after the antenna-base phase calibration of these three antennas using the reference antenna ***r***, which can be expressed as ϕ_{1r}, ϕ_{2r}, and ϕ_{3r} in Figure 4.5a. Since all these phases are measured relative to the phase of the reference antenna ***r***, the observed signals can be written as

$$\phi_{1r} = \phi_1 - \phi_r , \tag{4.2}$$

$$\phi_{2r} = \phi_2 - \phi_r , \tag{4.3}$$

$$\phi_{3r} = \phi_3 - \phi_r , \tag{4.4}$$

where ϕ_r and ϕ_1, ϕ_2, ϕ_3 are the actual phases at the reference antenna ***r*** and the three antennas of our reference triangle, respectively. We then consider the phase for the interpolated or extrapolated antenna ***t***. The actual and the observed phases for antenna ***t*** can be expressed as ϕ_t and ϕ_{tr}. The phases for the relation between ϕ_t

and ϕ_{tr} can be written as,

$$\phi_{tr} = \phi_t - \phi_r . \tag{4.5}$$

Now, we redefine the phase, which is, not measure from the reference antenna ***r***, but from the center of the triangle (see Fig. 4.5b). First, we define $\bar{\phi}$ as

$$\bar{\phi} \equiv (\phi_{1r} + \phi_{2r} + \phi_{3r})/3 = (\phi_1 + \phi_2 + \phi_3)/3 - \phi_r . \tag{4.6}$$

We can consider this phase as the phase of the center of the triangle relative to the reference antenna ***r***. If we subtract the phase $\bar{\phi}$ from other phases, these phases will be the phases refer to the center of the triangle. If we derive the phase of antenna ***t*** relative to the center of the reference triangle, the phase can be rewritten as

$$\phi_{tr} - \bar{\phi} = \phi_t - \phi_r - \bar{\phi} \tag{4.7}$$

If we substitute $\bar{\phi}$ in Eq.(4.6) into this equation, the equation can be written as

$$\phi_{tr} - \bar{\phi} = \phi_t - \phi_r - \left[(\phi_1 + \phi_2 + \phi_3)/3 - \phi_r\right] \tag{4.8}$$

$$= \phi_t - (\phi_1 + \phi_2 + \phi_3)/3 \tag{4.9}$$

The final form of this equation does not include the phase of the reference antenna ϕ_r, and only depends on the real phase of the target antenna ϕ_t relative to the real phase of the center of the triangle, $(\phi_1 + \phi_2 + \phi_3)/3$.

4.3 Comparison between Real and Subtracted Phase Fluctuations

We then compare the relationship between the spatial length to the center of reference triangle and the corrected phase fluctuations, which is depicted in Figure 4.6 to Figure 4.9. We separated the interpolated and extrapolated antennas, and also separated the large and small phase fluctuation data for each dataset (see Table 4.1). All the real phase fluctuations before the phase correction increase with the distance from the center of the reference triangle. The corrected (subtracted) phase, on the other hand, shows different behavior between the interpolated and extrapolated data.

The interpolated data show improvement in phase fluctuation, especially for the longer distance offset antennas. It seems that the phase correction efficiency depends mainly on center distance offset. Exception for this result is the first data (integration number of 140-199) of the dataset 040907 (Fig. 4.8a; see also Fig. 4.2a), which is largely affected by the 2π ambiguity. It is interesting to note that the data with more stable phase condition, the residual phase fluctuations get smaller.

The extrapolated data, on the other hand, show no improvement or often gets worse in phase fluctuation. Generally, the phase fluctuation increases with the distance from the center of the reference triangle. There is, however, a steep rise at the spatial length ρ around 60 meters and drop rapidly at longer ρ in all the subtracted phases of the extrapolation results (see Figs. 4.6b, 4.7b, 4.8b, and 4.9b). These data points are the extrapolated phases of antennas 2, 3, and 5 from reference triangle [2, 4, 6], [2, 4, 7] and [3, 4, 6]. We will discuss this later in Chapter 5.

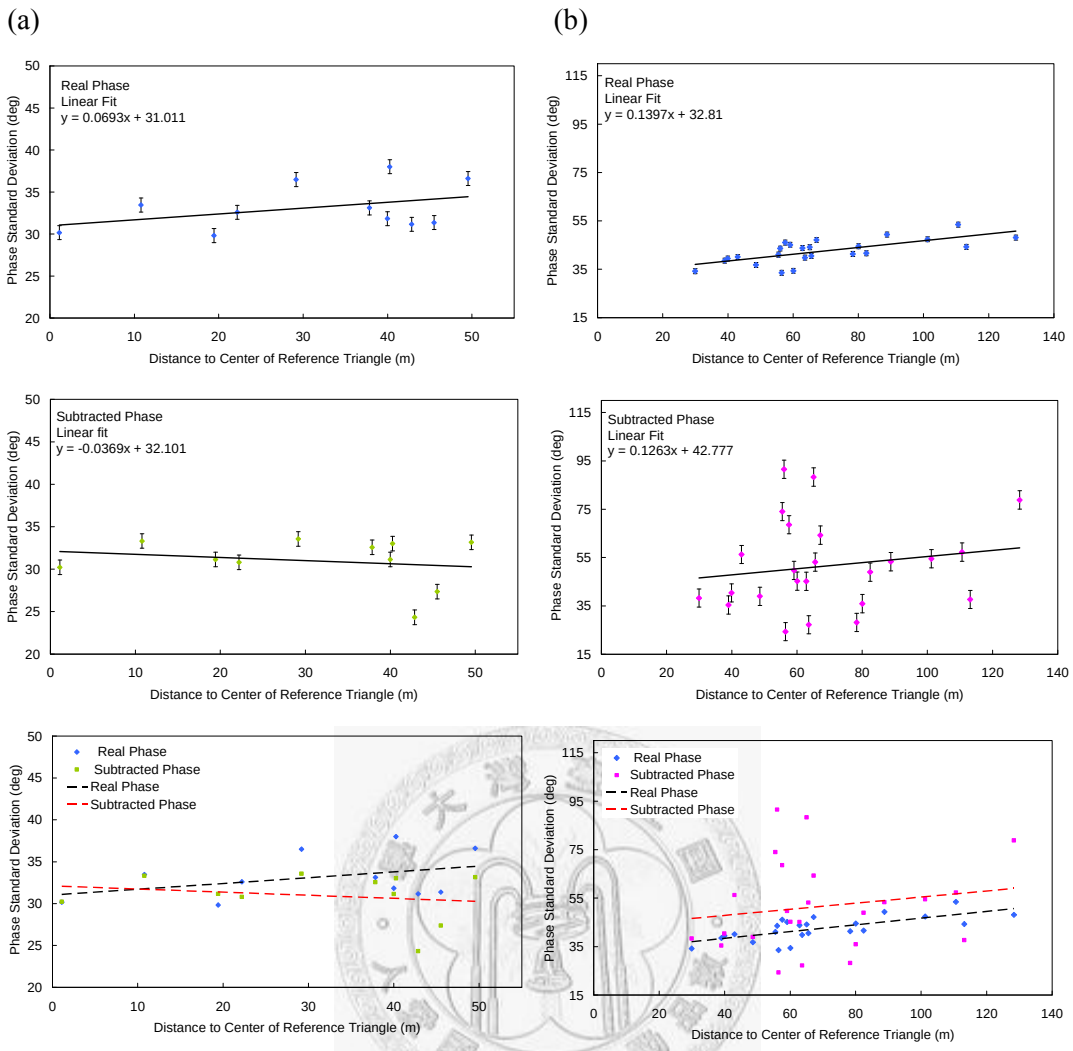

Figure 4.6 Plots of the real phase, interpolated phase, and the comparison between these two plots. (a) Interpolation results for time integration 2321-2799 of dataset 040826. (b) Extrapolation results for time integration 2321-2799 of dataset 040826. The error bar corresponds to one sigma error of the phase.

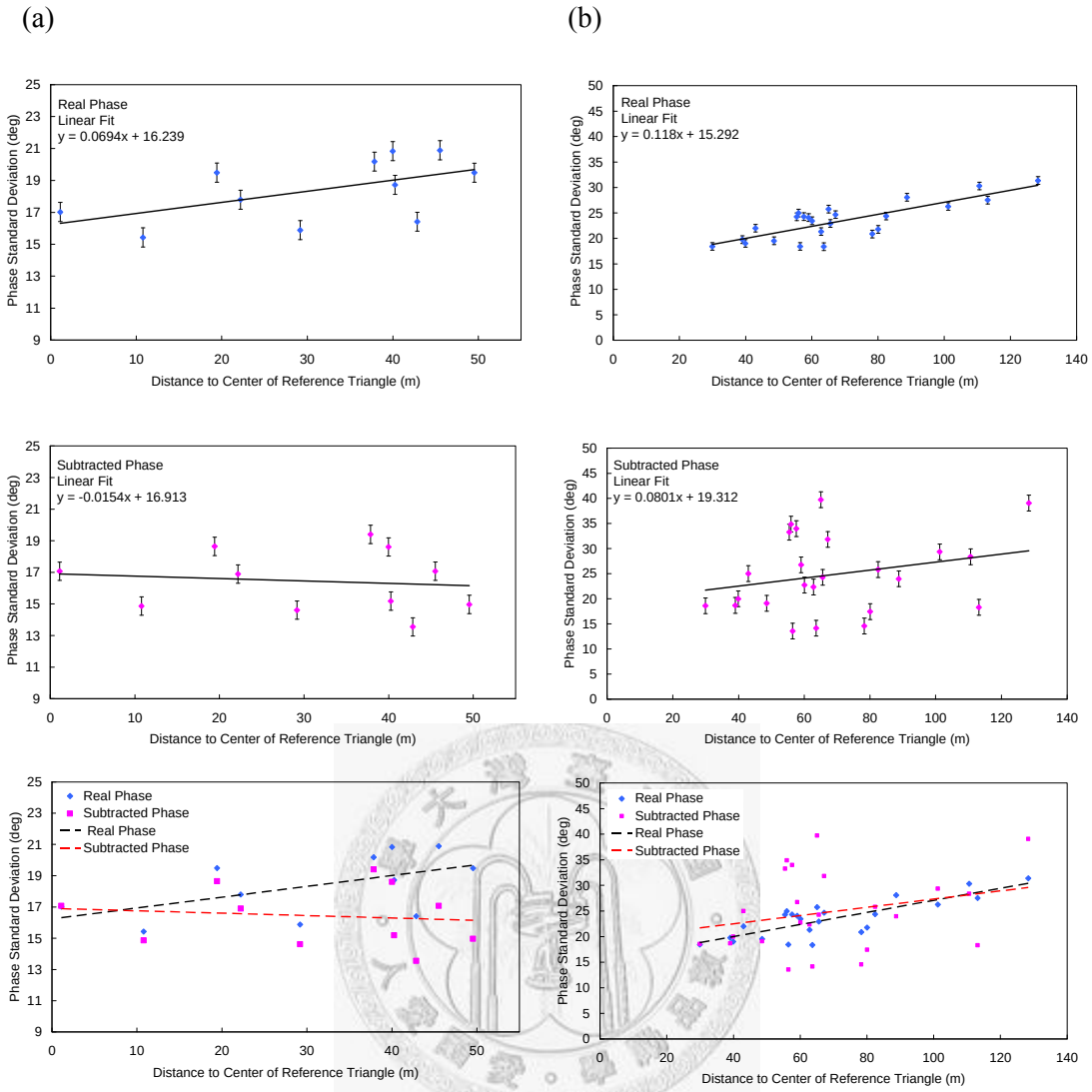

Figure 4.7 The same plots as in figure 4.6, but (a) interpolation results for time integration 2800-3128 of dataset 040826, and (b) extrapolation results for time integration 2800-3128 of dataset 040826.

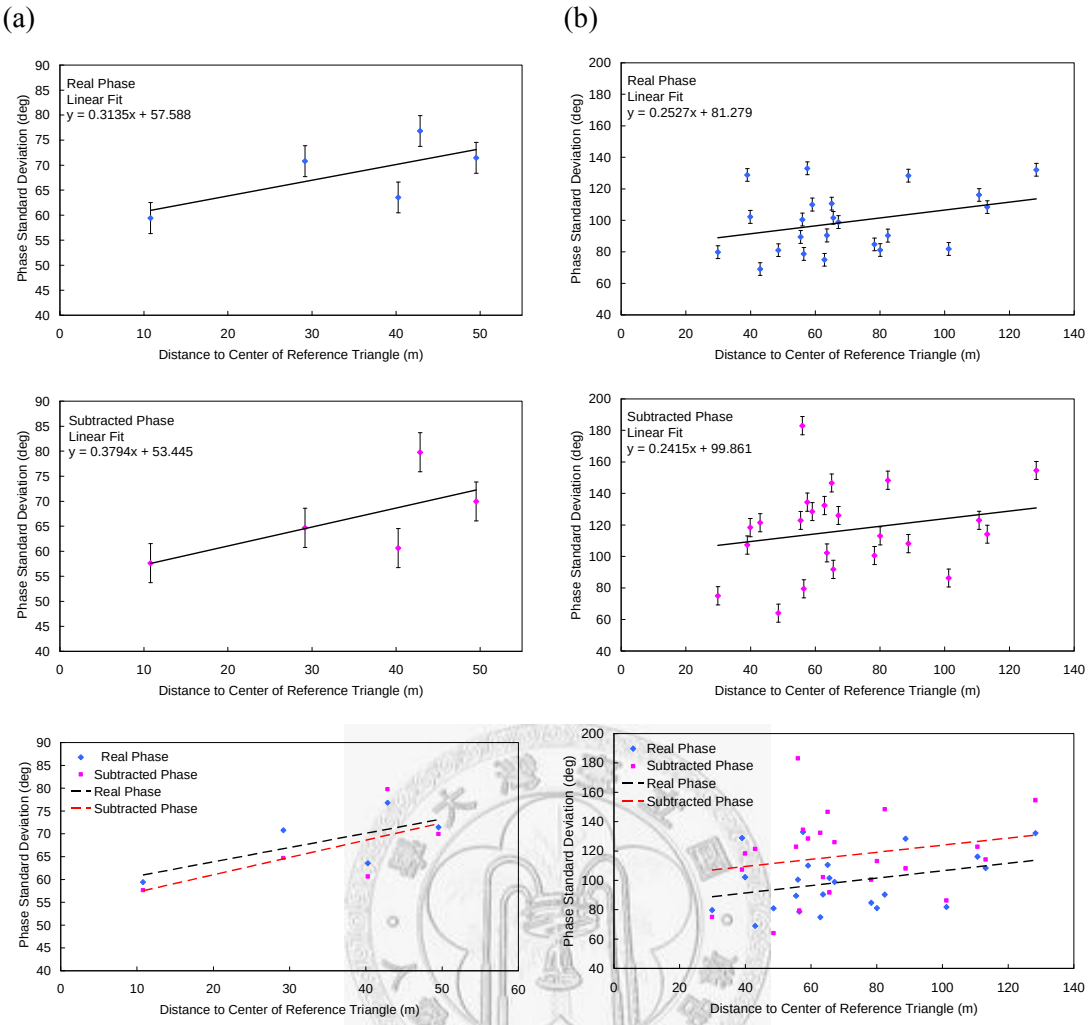

Figure 4.8 The same plots as in figure 4.6, but (a) interpolation results for time integration 140-199 of dataset 040907, and (b) extrapolation results for time integration 140-199 of dataset 040907.

(a) (b)

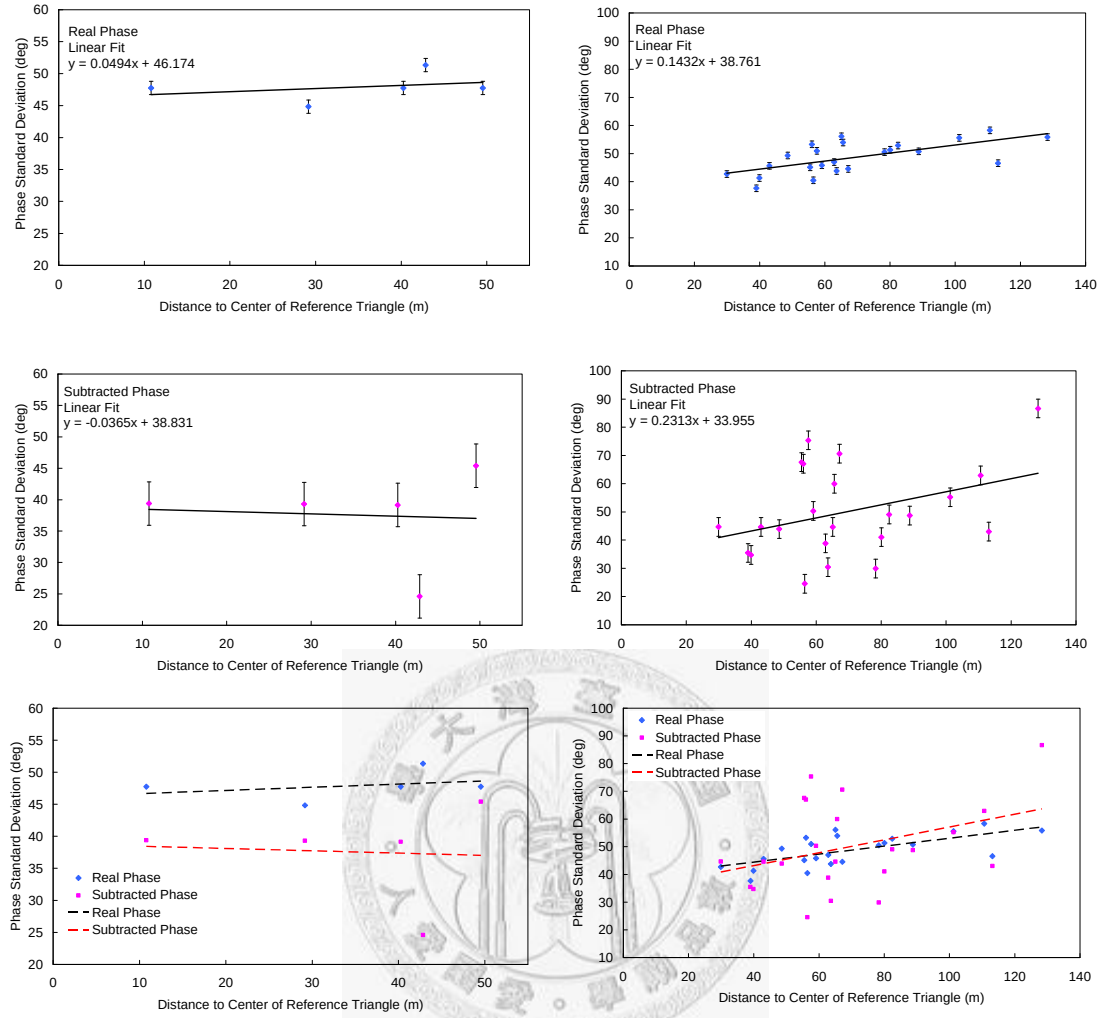

Figure 4.9 The same plots as in figure 4.6, but (a) interpolation results for time integration 200-467 of dataset 040907, and (b) extrapolation results for time integration 200-467 of dataset 040907.

4.4 Comparisons of RMS Phase with Temporal Structure Function

To evaluate the time variation of phase quantitatively, the temporal structure function is often used. Here, we define the temporal structure function $\mathcal{D}_\phi(\mathrm{T})$ as

$$\mathcal{D}_\phi(\mathrm{T}) \equiv \left\langle [\Phi(t+\mathrm{T}) - \Phi(t)]^2 \right\rangle, \tag{4.10}$$

where T is the characteristic integration time interval, and $\Phi(t)$ is the phase at integration time t. The angle bracket "$\langle\ \rangle$" means the time ensemble. We denote ϕ_{rms} as the root mean square (rms) of the temporal structure function $\sqrt{\mathcal{D}_\phi}$. We can compare ϕ_{rms} of the real phase with ϕ_{rms} of the interpolated/extrapolated phases as a function of integration time intervals. Figures 4.10 and 4.11 show the relation of root mean square temporal structure function of the real and residual phase.

The plots show that ϕ_{rms} rises with time interval T to a maximum value, and tend to be flat at this maximum value. If the maximum value for the subtracted phase gets lower than the real phase, the temporal structure function plots tell that the phase correction worked well. Indeed, in Figure 4.11, the interpolation scheme works most of the time, while the extrapolation scheme does not work well like the interpolation scheme. The extrapolation scheme sometimes works in short distances, but does not work in long distances. The effectiveness of the interpolation and extrapolation schemes is shown in Table 4.2.

The plots of the relation between the distance from the center of the reference triangle and the rms phase ($\sqrt{\mathcal{D}_\phi}$) with the different integration time interval are presented in Figures 4.12 and 4.13. Blue, pink, and green dots in the figures are 2, 10, and 20 integration time intervals, respectively. In all the integration time interval cases, longer integration time intervals tend to show larger phase fluctuation. In the case of the integration time interval of 2, the rms phase does not increase much with the spatial length ρ. The phases for the integration time interval more than 10 integrations, however, rise significantly with the spatial length ρ. Again, the phase variations have a sharply rise at the spatial length ρ around 60 meters.

(a) Interpolation (b) Extrapolation

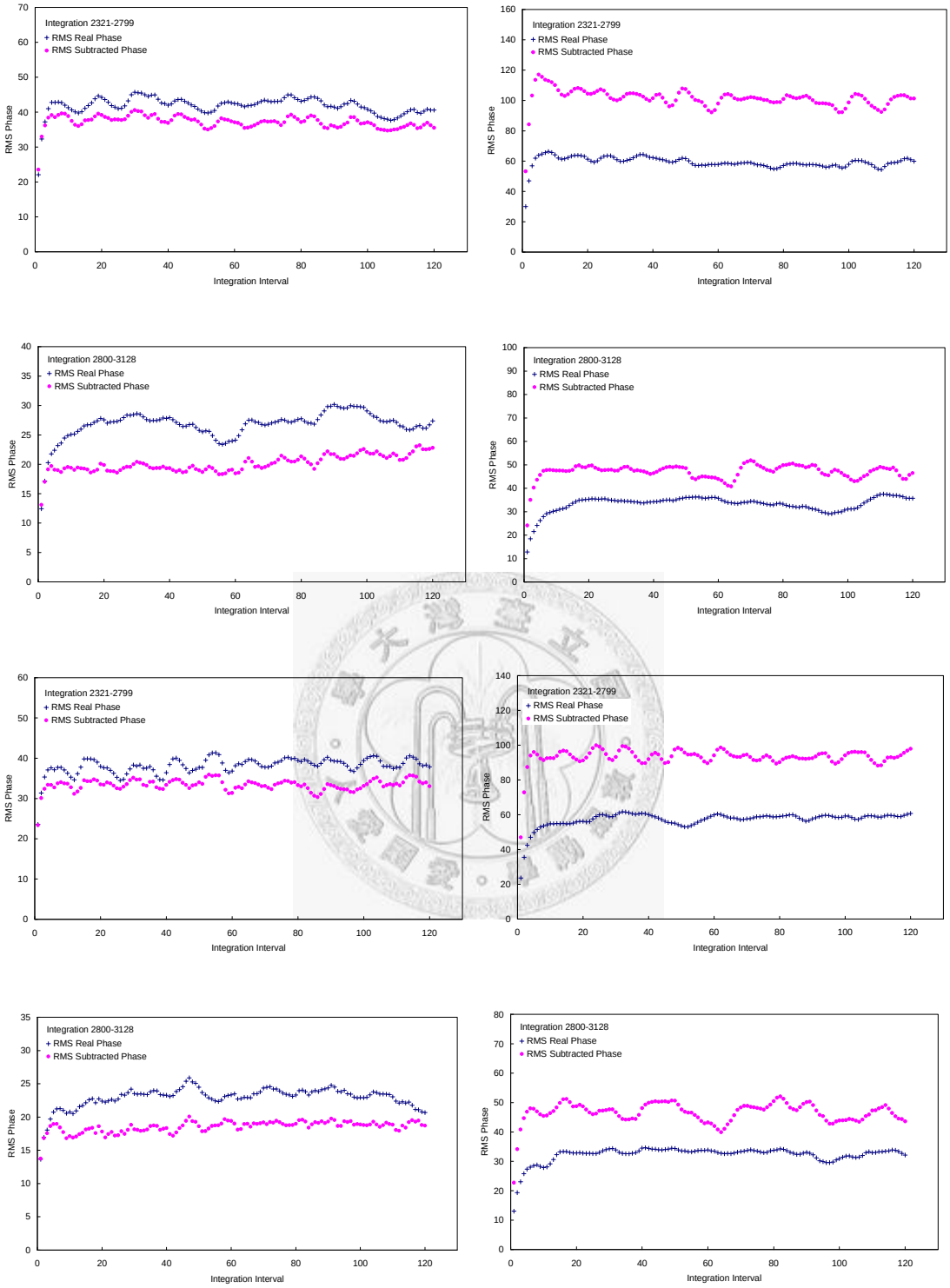

Figure 4.10 The root mean square temporal structure function of the real and subtracted phase from dataset 040826. (a) The interpolation results of the reference triangle [2, 4, 7] and [2, 5, 6] for antennas 8 and 7, respectively. (b) The extrapolation results of the reference triangle [2, 4, 7] and [2, 4, 6] for antennas 3 and 5, respectively.

(a) Interpolation (b) Extrapolation

Figure 4.11 Root mean square temporal structure function of the real and subtracted phase of the dataset 040907. (a) The interpolation results of the reference triangle [2, 3, 6] and [2, 5, 6] for antennas 1 and 7, respectively. (b) The extrapolation results of the reference triangle [2, 4, 7] and [2, 4, 6] for antennas 3 and 5, respectively.

Table 4.2 Effectiveness of the interpolation and extrapolation schemes

(a) Interpolation comparison of standard deviation for the real and subtracted phases.

Distance offset ρ (m)	Real phase rms (deg)	Subtracted phase rms (deg)
10.78813	47.74483	39.3843
29.17451	44.83473	39.3019
40.26273	47.74483	39.1590
42.84865	51.33642	24.5918
49.53231	47.74483	45.4089

(b) Extrapolation comparison of standard deviation for the real and subtracted phases.

Distance offset ρ (m)	Real phase rms (deg)	Subtracted phase rms (deg)
29.91766	79.77232	75.0352
38.9961	128.7902	107.2451
39.90832	102.179	118.3359
42.99792	69.0018	121.3851
48.58575	81.00795	64.0123
55.46777	89.4308	122.849
55.99502	100.488	182.9942
56.45395	78.71871	79.4144
57.56667	132.9996	134.451
59.06425	110.0124	128.4916
62.82648	74.95818	132.3584
63.63205	90.40502	102.2276
65.06253	110.583	146.6375
65.57583	101.5463	91.7562
67.17108	98.8503	125.987
78.29955	84.76246	100.5247
80.03234	81.13863	113.0428
82.4509	90.2943	148.3662
88.76965	128.323	108.1231
101.2208	81.86107	86.3214
110.6268	116.1609	122.9414
113.1465	108.3851	114.1335
128.3275	132.1032	154.5918

(a) Real phase integration = 2321-2799

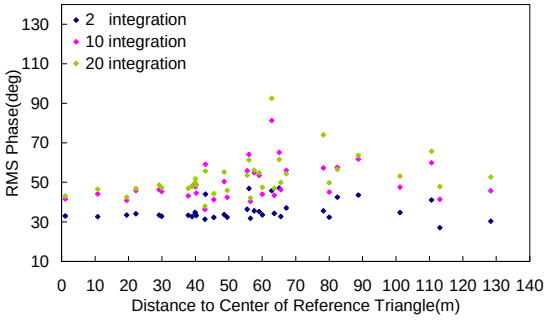

(b) Residual phase integration = 2321-2799

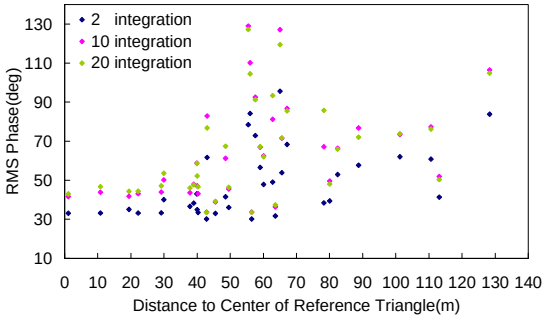

(c) Real phase integration = 2800-3128

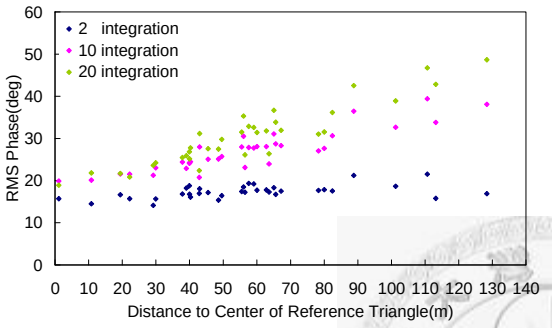

(d) Residual phase integration = 2800-3128

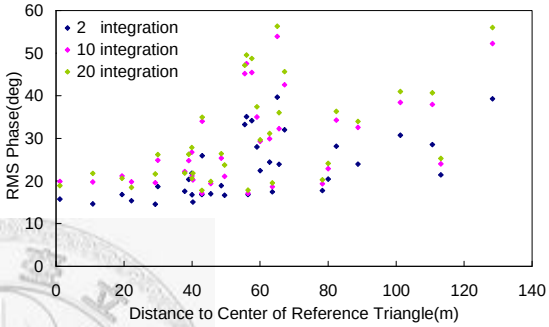

Figure 4.12 The relation between the distance to the center of reference triangle and the rms phase ($\sqrt{\mathcal{D}_\phi}$) with different integration time interval for the dataset 040826. Blue, pink and green dots in the figures are 2, 10, and 20 integration time intervals, respectively.

(a) Real phase integration = 140-199

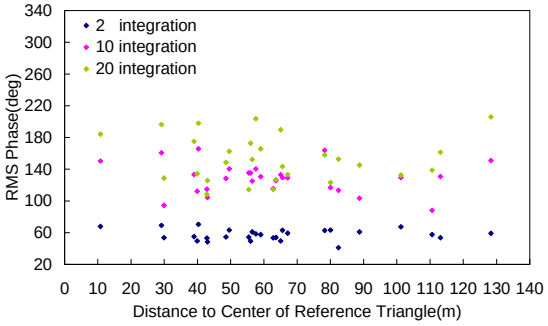

(b) Residual phase integration = 140-199

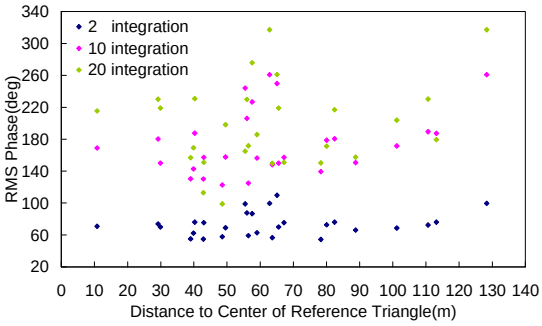

(c) Real phase integration = 200-467

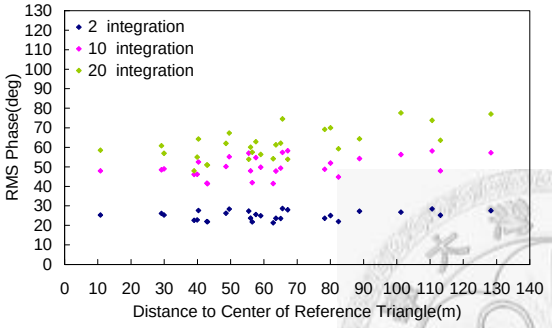

(d) Residual phase integration = 200-467

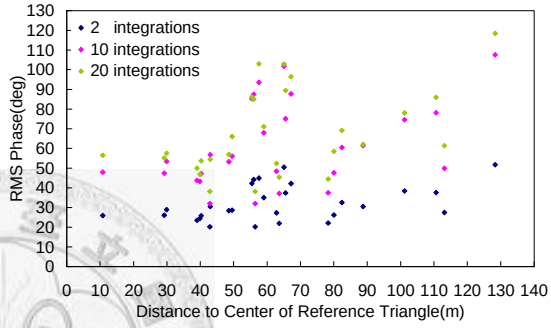

Figure 4.13 The relation between the distance to the center of reference triangle and the rms phase ($\sqrt{\mathcal{D}_\phi}$) with different integration time interval for the dataset 040907. Blue, pink and green dots in the figures are 2, 10, and 20 integration time intervals, respectively.

Chapter 5
Discussion

This study is to determine the efficiency of the interpolation or extrapolation phase compensation using phase screens for millimeter and submillimeter interferometer, especially for the ACA in the ALMA. In the previous chapter, we showed that the interpolation scheme outperforms the extrapolation one, suggesting that there is a merit to manipulate the interpolated phase correction.

5.1 Interpolation and Extrapolation

The results of experiments show that the phase interpolation provides a better estimation than the extrapolation approach. Considering it mathematically, the results of interpolation are calculated under the three boundary conditions of the three antenna phases as a reference triangle, while the results of extrapolation are calculated from the three initial conditions of the distribution of the phases. The difference between these two schemes can be compared in Figure 5.1. The interpolated phases are within confines of the reference antennas. The extrapolated phases are estimated from the phases of the reference antennas without any confine to be a boundary condition, therefore the extrapolation results deviate more than the interpolation results due to more degree of freedom or more uncertainties.

Furthermore, the distortion of the wave front is caused by the variations of the water vapor distribution in the troposphere that move across an interferometer. The situation between the atmosphere and the interferometer is depicted in Figure 5.2. Smaller scale water vapor “clumps” cause a smaller phase variations, and larger scale “clumps” cause a larger phase variations. Since the interpolation scheme is calculated within the separation of the reference antennas, the fluctuations of the phase variation (i.e., the size distribution of the water vapor clumps) are small. It is therefore possible to estimate a rough phase screen similar to the variation of phase, and compensate the phase fluctuation well.

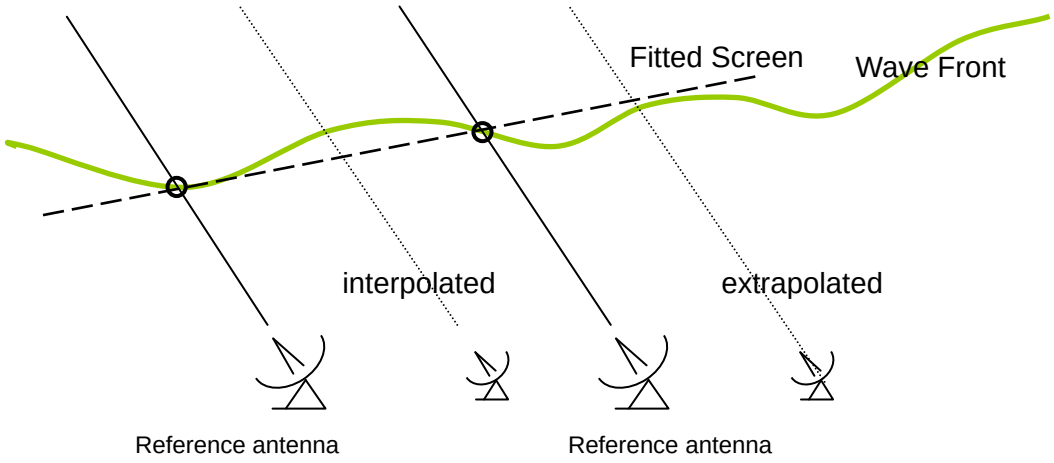

Figure 5.1 The wavefront corrected by the fitted screen. The interpolation estimations have three reference antennas being the "two-side" boundary condition, while the extrapolation estimations only have "one-side" boundary condition.

On the other hand, since the extrapolation scheme is calculated without any outer boundary condition, there is no limit on the size of the water vapor clumps, and therefore resulted as a large variation of phase (larger the distance from the center of the reference triangle, large the phase variations).

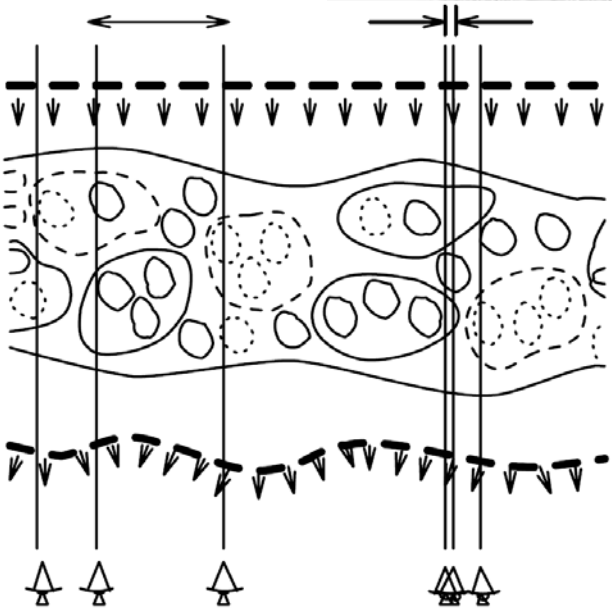

Figure 5.2 Cartoon showing the water vapor clumps with different scales (Carilli and Holdaway 1999).

5.2 Extraordinary 60-meter Fluctuations

In usual cases, the phase fluctuation increases with the increase of the spatial length, which is the distance from the center of the reference triangle to the interpolated or extrapolated antennas. However, as is shown in Figures 4.6 to 4.9, the subtracted phase of the extrapolation scheme suddenly goes up around the spatial length of 60 meters ($\rho \approx 60$ meters), much more than the general trend of the increase of the phase fluctuation. Figures 4.12 and 4.13 show another estimation of the stability of the phase, and the "60-meter phase fluctuation" can also be found easily in the residual (subtracted) plots. Different data points for ρ of 60-meter is from the different configurations of the reference triangles, and some follow the increasing trend, while some do not.

The difference is the orientation (direction) of the center of the reference triangle to the antennas. Depending on the orientation, the subtracted results can have entirely different phase fluctuations. Figure 5.3 presents the configurations of the reference triangles for two of those extraordinarily violent phase variation; antennas 2 and 3 in the reference triangle [3, 4, 7] and [2, 4, 7]. The extraordinary 60-meter phase fluctuation data all have similar orientation of ρ, which is almost along the north-south direction. The meteorological parameters on these two days show that the prevailing wind direction is either east or west (Figs. 5.4a and 5.4b). These are almost perpendicular to the orientation of ρ with extraordinary 60-meter fluctuations on both days (Fig. 5.3). Note that in most cases at the summit of Mauna Kea, the wind direction is either east or west (Fig. 5.5). We have a possible explanation for this extraordinary phenomenon.

The time variations of the atmospheric phase are usually approximated by a "frozen screen" model proposed by Taylor (1938) and Garratt (1992), in which the turbulence as 'frozen' and assuming that a uniform wind is translating the air mass with water vapor in scale height 2 km across the antennas (Léna et al. 1998). The physical origin of the Taylor's hypothesis is that the time scales involving development of turbulence are much longer than the time taken for a turbulent field removed or displaced by wind to pass across the aperture of a telescope or an interferometer. In general case, the phase fluctuation in an interferometer can be explained by this effect (Figure 5.6).

Since the wind direction and the orientation of ρ of the extrapolated antenna are almost perpendicular, the "60-meter phase fluctuation" suggests that the extrapolation of phase for direction perpendicular to the wind direction cannot be well modeled the frozen flow with the phase screen phase correction method.

(a)

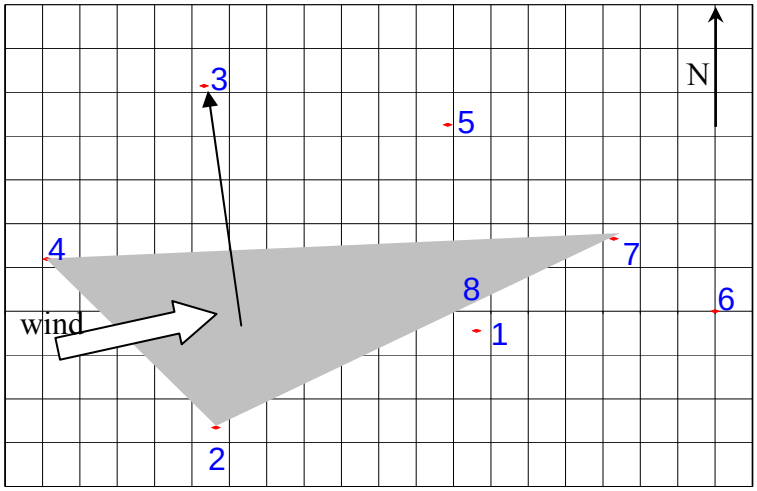

(b)

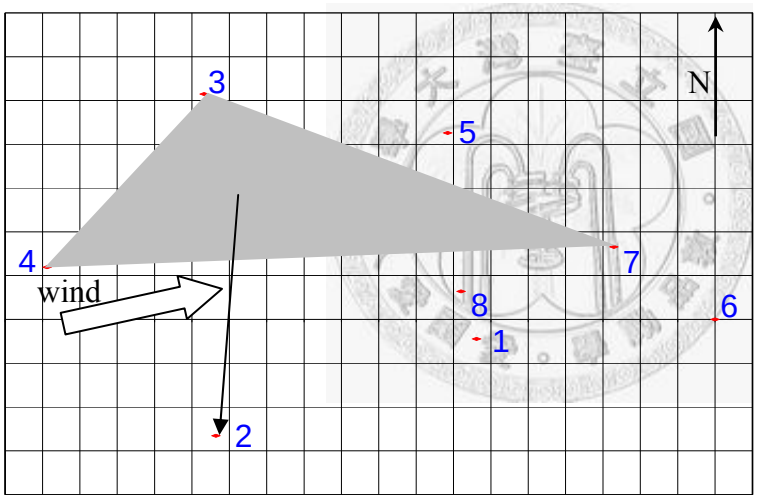

Figure 5.3 Schematic diagram of the phase surface created by the reference antennas and the distance from the center of the reference triangle to the extrapolated antenna (ρ). The unit length of the grid is 10 meters. The black arrow in each diagram shows an example of ρ of around 60 meters. The white arrow is the direction of the prevailing wind. (a) The reference triangle is composed of antennas 2, 4, and 7. The subtracted phase of the extrapolated antenna 3 rises extraordinarily. (b) Another configuration of the reference triangle [3, 4, 7]. The antenna 2 has an extraordinary rise of the subtracted phase.

(a)

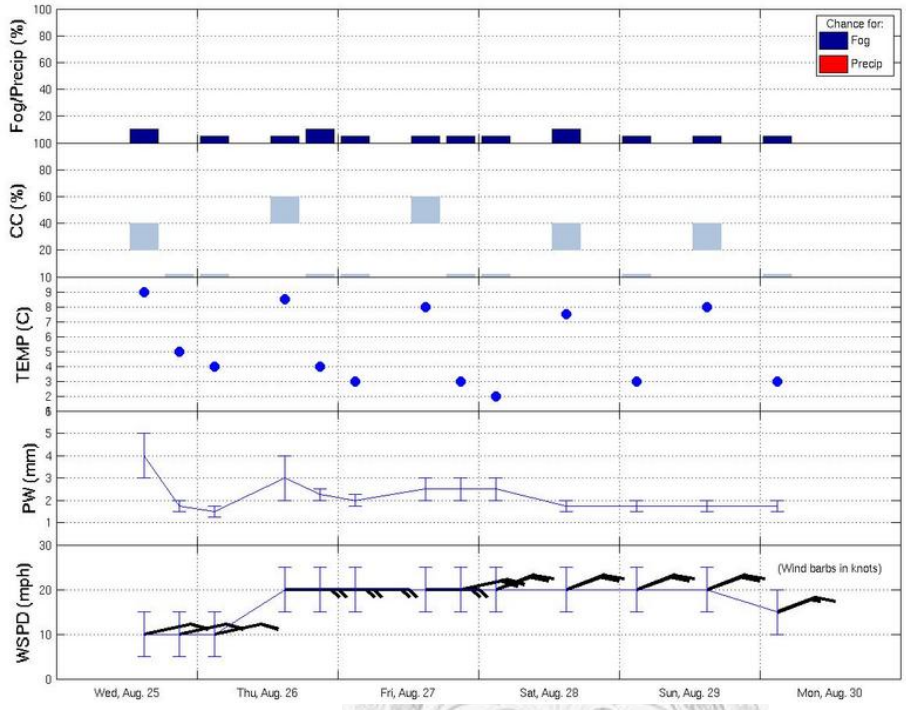

(b)

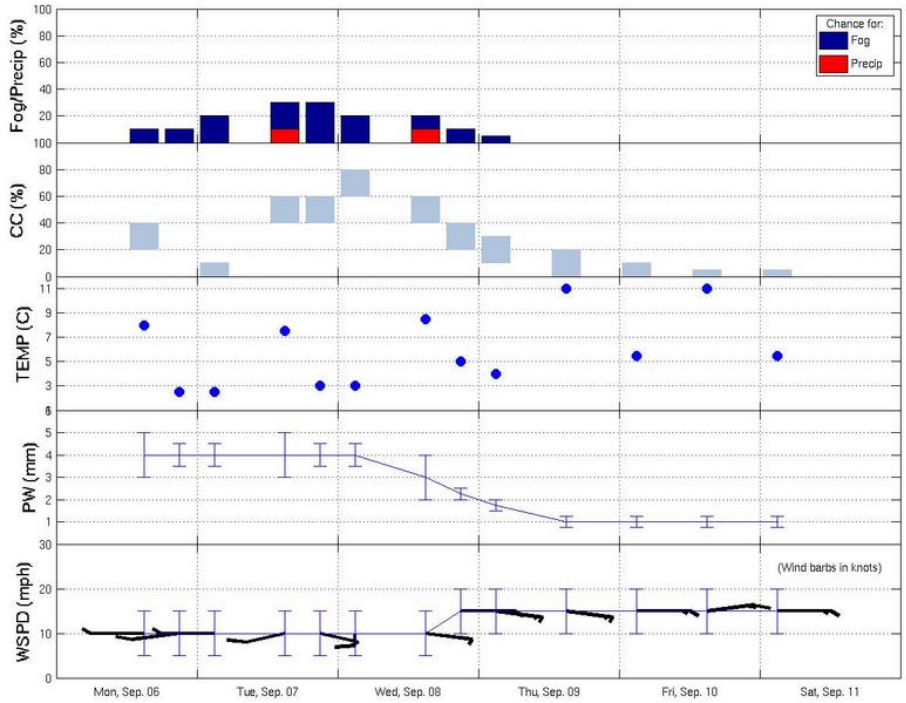

Figure 5.4 The meteorological parameters of (a) Aug. 26, 2004, and (b) Sep. 07, 2004 on Mauna Kea. "PW" is the precipitable water and "WSPD" is the wind speed. The surface wind direction is mostly east on this day. The plot is from the MKWC forecast.

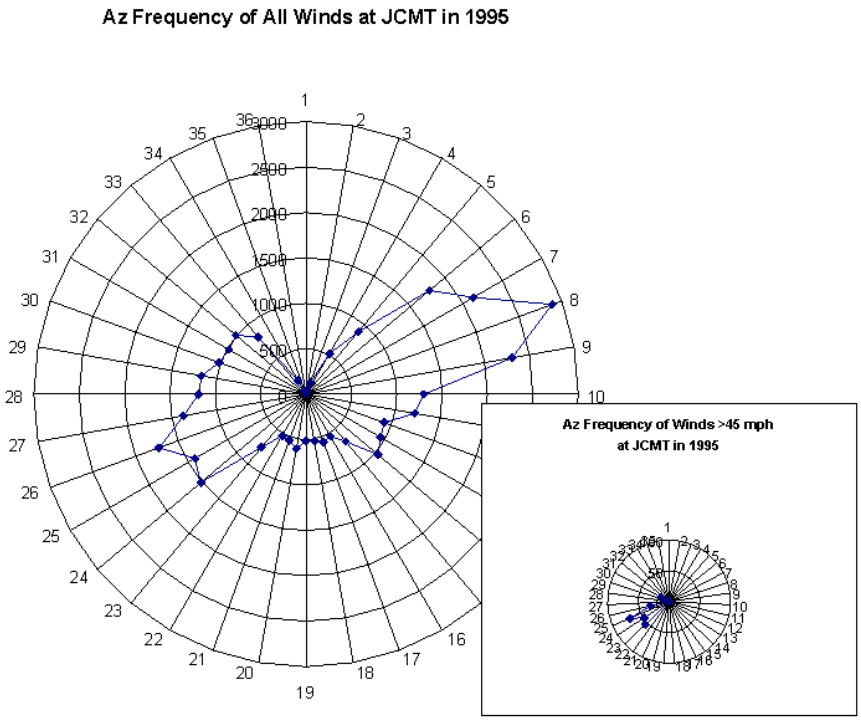

Figure 5.5 Azimuth wind direction frequency of all winds at the JCMT on the summit of Mauna Kea in 1995.

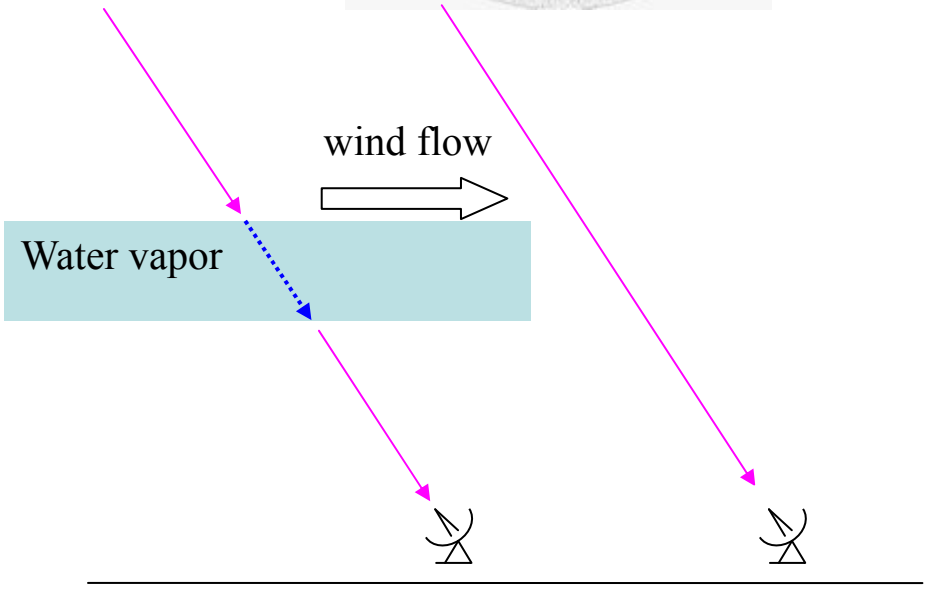

Figure 5.6 The schematic diagram of the "frozen screen" model. The water vapor content moves with the wind aloft.

In the boundary layer of the Earth, since the upper air wind is stronger with less friction compared to the surface wind, the atmospheric effect of the surface friction by the wind aloft forces the surface wind to slow down. Over a rough terrain, the wind gradient effect could cause a reduction of 40% to 50% of the geostrophic wind speed aloft (Thompson and Russell 1998). The surface wind speed of Aug. 26, 2004 and Sep. 07, 2004 were 9 m s^{-1} (20 mph) and 4 m s^{-1} (10 mph), respectively (Tables 5.1 and 5.2). But due to the effect mentioned above, the strength of the wind advection speed may not be negligible, and the upper wind can be stronger than 10 m s^{-1}. Figure 5.8 shows a schematic diagram and a table of the difference in wind speed as a function of height. The table shows that the wind speed will be more than two times larger than the wind speed at the surface. The wind aloft on these measurement days may therefore be stronger and affect more than the wind flow velocity adopted by Asaki et al. (2005). They suggested that the upper air wind speed less than 10 m s^{-1} do not affect the phase fluctuations. Since the stronger wind may cause more phase fluctuations, the phase error due to water vapor advection of specified wind direction may lead to difficulty in the extrapolation phase correction scheme under a longer time scale and a stronger wind field, and cause the sudden augment of phase fluctuations corresponding to the "60-meter phase fluctuation".

In addition, the wind flows more northern or southern direction due to the Coriolis force. Figure 5.7 also shows a change of the wind direction due to the Coriolis force. The wind direction can be changed for a few tens of degrees for the water vapor scale height of 2 km.

The location of the SMA is, on the other hand, at the top of Mauna Kea, which has less surface area than the ground at the sea level. These effects may therefore be small. To make this point clear, we need more careful inspection of the metrological data around Mauna Kea.

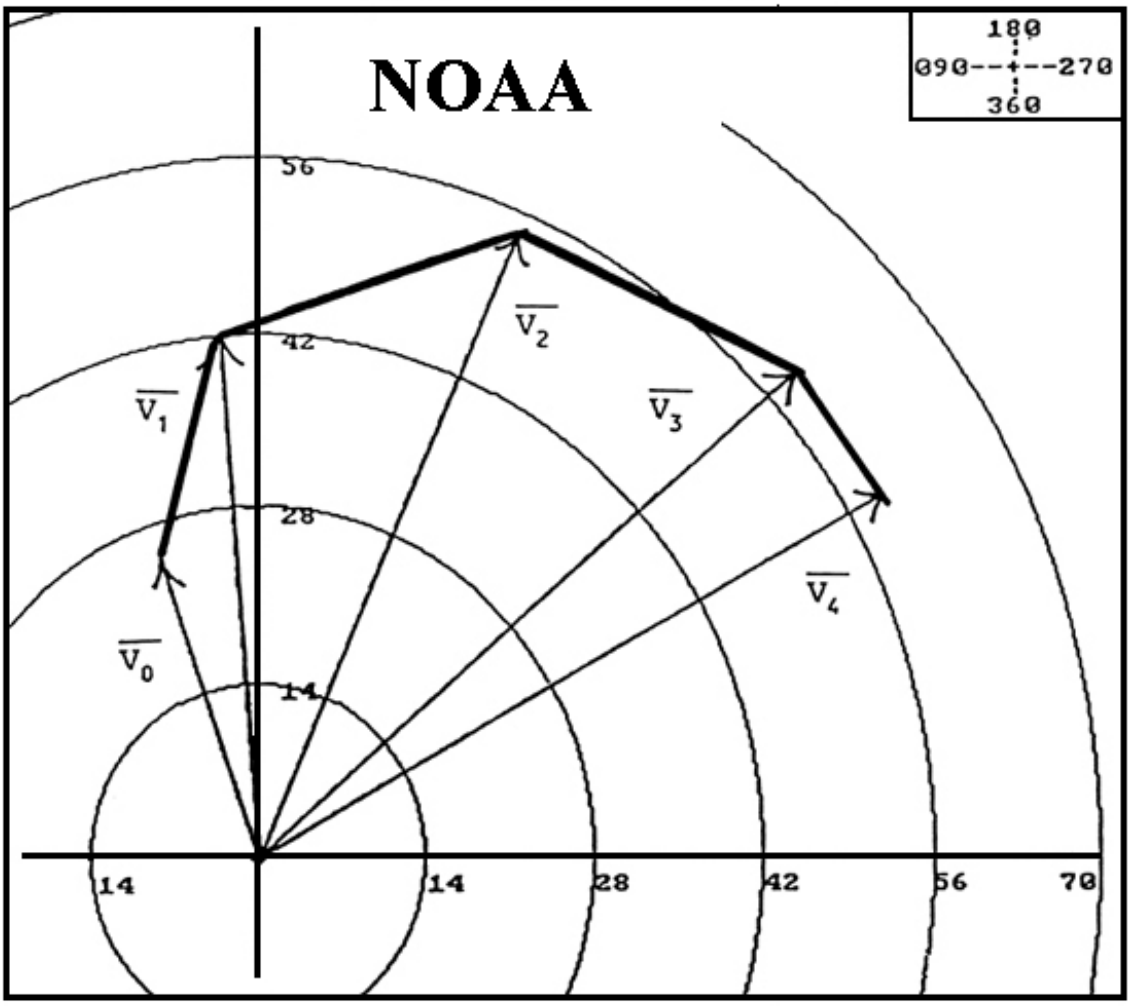

Winds / Vents

Height / Hauteur (km)	Dir	Speed / Vitesse
Sfc	161°	25
1	175°	42
2	204°	54
3	229°	59
4	241°	59

Figure 5.7 Schematic diagram of hodograph plot of wind vectors at various heights in the troposphere. Meteorologists can use this plot to evaluate vertical wind shear in weather forecasting. The wind speed gradient is caused by the boundary layer friction and the wind direction is affected by the Ekman effect due to the Coriolis force (source: NOAA).

Table 5.1 Wind velocity (m s^{-1}) at 200 mb obtained from the NOAA GGUAS data base (Carrasco and Sarazin 2003).

M	Costa Rica		SPM		Mauna Kea		Paranal		La Silla		La Palma		Gamsberg		Maidanak	
	Ave	rms	Ave	rms	Ave	rms	Ave	rms	Ave	rms	Ave	rms	Ave	rms	Ave	rms
1	14.2	7.1	33.7	14.7	30.6	11.8	19.5	7.7	27.2	10.0	20.9	10.2	13.6	6.7	28.6	10.2
2	14.1	6.9	37.1	14.7	34.3	11.9	19.3	8.3	24.6	10.4	24.0	10.9	12.2	6.5	27.9	12.5
3	12.5	6.8	39.5	15.6	34.6	13.5	22.0	8.7	26.4	11.3	25.7	13.8	18.5	8.4	27.2	10.6
4	10.8	5.9	31.2	14.6	33.5	14.6	29.7	10.7	31.7	12.8	29.2	13.4	28.7	12.5	24.9	10.0
5	7.8	4.3	27.6	13.7	27.7	13.5	35.5	14.5	36.2	14.3	27.9	12.7	30.2	12.0	26.5	10.6
6	8.1	4.4	21.6	11.0	21.4	11.2	35.6	14.6	36.0	14.1	22.9	10.3	33.0	12.4	30.8	12.3
7	7.6	4.0	11.3	6.9	18.7	8.6	37.4	14.8	37.7	15.6	16.2	8.6	32.1	11.8	27.3	9.7
8	8.1	4.2	12.1	6.4	16.8	7.9	36.2	12.6	38.1	14.4	15.7	8.1	29.9	11.8	28.9	10.4
9	7.6	4.0	19.7	10.2	19.1	8.0	36.6	13.8	36.3	13.8	18.2	9.1	25.6	10.7	30.2	11.0
10	7.8	4.2	27.4	12.0	21.1	9.2	35.8	11.3	39.2	13.1	19.5	10.6	26.6	10.4	25.0	11.9
11	8.3	4.4	30.4	13.8	20.8	10.7	30.9	10.0	34.0	12.8	23.9	11.0	24.0	9.4	28.2	11.1
12	12.2	5.7	32.9	14.0	26.5	11.4	24.5	9.9	27.6	11.7	21.3	11.4	20.9	9.5	27.3	11.3
Ave	**9.9**	5.3	**27.0**	12.6	**25.4**	11.2	**30.3**	11.7	**32.9**	12.9	**22.1**	10.9	**24.6**	10.4	**27.7**	11.0

Table 5.2 Wind velocity (m s^{-1}) at 200 mb obtained from the NOAA NCEP data base (Carrasco and Sarazin 2003).

M	Costa Rica		SPM		Mauna Kea		Paranal		La Silla		La Palma		Gamsberg		Maidanak	
	Ave	rms	Ave	rms	Ave	rms	Ave	rms	Ave	rms	Ave	rms	Ave	rms	Ave	rms
1	13.9	3.1	32.2	4.8	29.9	4.9	18.5	2.8	27.2	4.3	20.3	4.0	12.4	2.8	33.2	5.9
2	13.2	2.7	35.8	7.1	32.9	4.4	18.2	3.5	24.1	4.1	24.1	4.4	10.2	2.9	33.1	7.4
3	12.0	3.5	38.4	9.0	33.5	5.4	20.6	3.5	25.9	4.7	25.9	6.2	17.5	3.5	31.1	4.3
4	9.4	2.9	30.2	8.3	32.0	5.9	28.3	3.2	30.6	4.8	29.0	4.8	27.3	4.6	26.5	4.6
5	7.1	1.3	28.7	7.1	25.0	5.7	33.9	5.3	35.6	5.2	27.4	5.4	29.3	2.9	29.3	5.3
6	8.7	2.1	20.9	4.6	20.7	5.3	36.5	6.2	35.1	5.7	21.4	4.2	31.7	4.3	31.5	4.4
7	8.4	2.0	10.5	3.2	18.2	3.3	36.7	6.3	36.9	5.6	15.7	3.9	31.5	4.6	22.2	5.4
8	9.9	2.3	11.9	2.5	15.8	2.2	35.6	5.6	37.4	7.0	14.9	2.5	28.8	4.4	23.6	6.5
9	8.9	1.7	19.7	4.6	18.1	3.3	35.9	7.2	34.8	4.7	17.1	2.7	24.6	2.9	29.4	4.8
10	9.1	1.8	26.8	4.4	19.5	3.3	34.9	3.2	38.2	4.1	18.81	3.8	25.0	2.8	27.4	5.0
11	8.4	2.4	30.4	5.4	20.6	4.6	29.2	3.5	34.0	6.3	21.8	4.2	22.2	3.7	31.0	4.2
12	12.0	2.7	32.1	6.3	25.4	4.8	23.5	3.4	34.0	6.3	20.2	5.3	18.9	2.8	31.3	5.1
Ave	**10.1**	2.4	**26.5**	5.9	**24.3**	4.5	**29.3**	4.7	**32.4**	5.2	**21.4**	4.4	**23.3**	3.6	**29.1**	5.3

Chapter 6
Conclusions

We performed an interferometric phase correction at millimeter and submillimeter wavelengths with the interpolation or extrapolation of the phase screen defined by three reference antennas using the SMA. This interpolation method is proposed for the ACA in the ALMA, and our results reported here can provide the evaluation of this phase correction scheme. Here are the summary of our results and discussions.

- According to the comparisons of the standard deviations of residual (subtracted) phases, relations between the rms phase and the distance from the center of the reference triangle, and the temporal structure function of the rms phase, the interpolation scheme improves phase fluctuation while the extrapolation scheme does not.
- This result can be explained by the boundary conditions of phase in these schemes; in case of the interpolation scheme, the phase corrected antenna is inside the triangle of three reference antennas, so the phase inside the triangle can be well defined (more known boundary conditions, more precisions or less phase errors and deviations). The extrapolation scheme, on the other hand, only has partial boundary conditions, and therefore less precision.
- However, too large phase fluctuations due to tropospheric water vapor content cannot have good phase correction results. This is largely due to the 2π ambiguity of the phase.
- In the extrapolation scheme results, there is a sudden large phase fluctuation around the distance from the center of the reference triangle of 60 meters. According to the meteorological parameters on those observing dates and the antenna configurations, this “60-meter phase fluctuation” is occurring only at the antennas located from the center of the reference triangle perpendicular to the wind direction.
- This “60-meter phase fluctuation” can be explained by the frozen flow model. The extrapolation scheme has only partial boundary conditions of phase, and especially in this case, the boundary condition is located far from the extrapolated antenna and perpendicular to the wind direction. The phase information (water vapor clumps) flows as the wind flows, but in this case, the

phase information cannot be used due to this special antenna configuration, and therefore the phase correction scheme does not work at all.

- In our two measurement dates, the wind speeds were around 4 and 9 m s^{-1}. In Asaki et al. (2005), there is no difference in the results of the phase correction between the upper air wind strength of 5 and 10 m s^{-1}. But in our case, the wind speed can be much higher at the upper air, if we consider the surface friction effect. We need more meteorological inspection around the summit of Mauna Kea to see whether this affects the results.

Reference

Asaki, Y., Saito, M., Kawabe, R., Morita, K.-I., Sasao, T. Radio Science, 31, 1615, 1996

Asaki,Y., Shibata, K. M., Kawabe, R., Roh, D.G., Saito, M., Morita, K.-I., and Sasao, T., Radio Science, 33, 1297, 1998

Asaki, Y., Saito, M., Kawabe, R., Morita, K. I., Tamura,Y. and Baltasar, V.-V., ALMA Memo. No. 535, 2005

Carilli, C. L. and Holdaway, M., ALMA Memo No.262, 1999

Carilli, C. L., Carlstrom, J. E., and Holdaway, M. A., in *Synthesis Imaging in Radio Astronomy II*, ed. G. B. Taylor, C. L. Carilli, and R. A. Perley, Astronomical Society of the Pacific Conference Series, Vol. 180, 565, 1998

Crane, R. P., in *Methods of experimental physics*, vol. 12B: Radio Telescopes, ed. M. L. Meekes (Academic Press: New York), 186, 1976

Carrasco, E. and Marc, M. S., RevMexAA (Serie de Conferencias), 19, 103, 2003

Hess, S. L., *Introduction to Theoretical Meteorology*, 1959

Ho. P., Moran, J. and Lo, K. Y., ApJ, 616, L1, 2004

Holdaway, M., ALMA Memo No.491, 2004

Humphreys, W. J., *Physics of the Air*, 3rd ed., (McGraw-Hill: New York), 1940

Jackson, J. D., *Classical Electrodynamics*, 3rd ed. (John Wiley and Sons: New York), 1998

Léna, P., Lebrun, F., Mignard, *Observational Astrophysics* 2nd ed. (Springer-Verlag, Berlin), 1998

Liebe, H. J., International Journal of Infrared and Millimeter Waves, 10, 6, 1989

McKinnon, M. M., MMA Memo No.49, 1988

Reber, E. E., and Swope, J. R., J. Appl. Met., 11, 1322, 1972

Smith, E. K., Jr., and Weintraub, S., Proc. IRE (Inst. Radio. Eng.), 41, 1035, 1953

Sutton, E. C., and Hueckstaedt, R. M., A&A Supp., 119, 559, 1997

Tatarskii, V.I., *Wave Propagation in Turbulent Media* (Wiley and Sons: New York), 1961

Taylor, G. B., Carilli,C. L., and Perley, R. A., *Synthesis Imaging in Radio Astronomy II*, Astronomical Society of the Pacific Conference Series, Vol. 180, 1998

Taylor, G. I., Proc. R. Soc. London Set A, 164, 476, 1938

Garratt, J. R., in *The Atmospheric Boundary Layer* (Cambridge University Press: Cambridge), 11, 1992

Thompson A, R., Moran J. M., & Swenson G. W., Jr., *Interferometry and Synthesis in Radio Astronomy,* (Wiley-Interscience), 1986

Thompson, R. D., *Atmospheric Processes and Systems* (Routledge: New York), 1998

Tornikoski, M., Valtaoja, E., Teräsranta, H., Karlamaa, K., Lainela, M., Nilsson, K., Kotilainen, J., Laine, S., Lähteenmäki, A., Knee, L. B. G. & Botti, L. C. L., A&AS, 116, 157, 1996

Wiedner, M., *183 GHz Radiometer for CSO-JCMT Interferometer*, Doctoral Thesis (Cambridge/MRAO), 1998

Wills, D., & Wills. B. J., Nature, 289, 384, 1981